




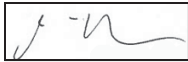
# ERROR PROPAGATION IN THE ATMOSPHERIC CORRECTION

---

DOCUMENT REF: S3-L2-SD-01-C01-ACR-TN\_OLCIACErrorPropagation  
DELIVERABLE REF: SD-01-C01-ACR-TN  
VERSION: 1.2  
CREATION DATE: 3 MAY 2010  
LAST MODIFIED: 30 SEPTEMBER 2010

	SENTINEL-3 OPTICAL PRODUCTS AND ALGORITHM DEFINITION  ERROR PROPAGATION IN THE ATMOSPHERE CORRECTION	REF: S3-L2-SD-01-C01-ACR-TN VERSION: 1.2 DATE: 30 SEPTEMBER 2010 PAGE I
--	---	--

#### DOCUMENT SIGNATURE TABLE

	NAME	FUNCTION	INSTITUTION	SIGNATURE AND DATE
PREPARED	Nicolas Lamquin	Research Engineer	ACRI-ST	
VERIFIED	A. Mangin	Research Engineer	ACRI-ST	
RELEASED	O. Fanton d'Andon	OLCI coordinator	ACRI-ST	

#### DOCUMENT CHANGE RECORD


VERSION	DATE	AUTHOR	DESCRIPTION
1.0	3 May 2010	ACRI-ST	Initial version
1.1	16 July 2010	ACRI-ST	Updated version including the description of error LUT generation
1.2	30 September 2010	ACRI-ST	Updated version including the new LUT generation algorithm and new comparison results

FROM <VERSION> TO <VERSION>

PAGE	SECTION	COMMENTS

#### DOCUMENT DIFFUSION LIST

ORGANISATION	NAME	QUANTITY
ESA	Philippe Goryl, Alessandra Buongiorno, Carla Santella	
EUMETSAT	Vincent Fournier-Sicre, Vincenzo Santacesaria	
S3 Optical team	ARGANS, ACRI-ST	

	<p>SENTINEL-3 OPTICAL PRODUCTS AND ALGORITHM DEFINITION</p> <p>ERROR PROPAGATION IN THE ATMOSPHERE CORRECTION</p>	<p>REF: S3-L2-SD-01-C01-ACR-TN</p> <p>VERSION: 1.2</p> <p>DATE: 30 SEPTEMBER 2010</p> <p>PAGE II</p>
--	---	--

## TABLE OF CONTENTS

LIST OF FIGURES.....	II
LIST OF TABLES .....	IV
1 INTRODUCTION.....	1
1.1 Scope.....	1
1.2 Purpose .....	1
1.3 References .....	2
1.3.1 <i>Applicable Documents</i> .....	2
1.3.2 <i>Reference Documents</i> .....	2
2 METHODOLOGY .....	3
2.1 MEGS data processing .....	3
2.2 Implementing a noise loop in the data processing.....	3
2.3 Scene selection .....	5
3 RESULTS OF A NOISE SIMULATION ON A SPECIFIC HALF-ORBIT .....	6
3.1 General statistics.....	6
3.1.1 <i>Diagonal models</i> .....	7
3.1.2 <i>General considerations</i> .....	8
3.2 Statistics on reflectances at 412 nm .....	15
3.3 Statistics on marine reflectances $\rho_w$ at 412 nm for distinct water types and aerosol couples 20	
4 NOISE SIMULATION ON 40 HALF-ORBITS, STATISTICS FOR DIFFERENT GEOMETRIES .....	25
4.1 General statistics.....	25
4.2 Statistics on marine reflectance at 412 nm for different geometry classes.....	26
4.2.1 <i>Statistics for diagonal couples</i> .....	27
4.2.2 <i>Statistics for non-diagonal couples</i> .....	27
5 LOOK-UP TABLES FOR UNCERTAINTY ESTIMATION.....	35
5.1 Method using the ( $\sigma_{pw}$ , $\rho_w$ ) histograms .....	35
5.2 Method using other variables.....	36
5.2.1 <i>Implementation of the method</i> .....	37
5.2.2 <i>Comparisons for stable couples over case 1 waters</i> .....	40
5.2.3 <i>Comparisons for all couples (stable + unstable) over case 1 waters</i> .....	43
5.2.4 <i>Comparisons for stable couples over turbid waters</i> .....	45
6 SYNTHESIS .....	48

## LIST OF FIGURES

Figure 1: Processing chart of data processing through MEGS.....	4
Figure 2: Occurrence frequencies of (model 1, model 2) couples of aerosol models along the half-orbit '20051227_035604' (%). With (left) and without (right) diagonal models.....	6
Figure 3: Relative differences between extrapolated and observed ratio at 775 nm for diagonal model 0 (left) and all other diagonal couples (middle). Relative difference of the bracketing aerosol ratio relatively to the observed ratio for non-diagonal couples (right).....	8
Figure 4: Statistical quantities derived from a noise loop over one pixel data. ....	10


	<p>SENTINEL-3 OPTICAL PRODUCTS AND ALGORITHM DEFINITION</p> <p>ERROR PROPAGATION IN THE ATMOSPHERE CORRECTION</p>	<p>REF: S3-L2-SD-01-C01-ACR-TN</p> <p>VERSION: 1.2</p> <p>DATE: 30 SEPTEMBER 2010</p> <p>PAGE III</p>
--	---	---

Figure 5: Histogram of NUM_STABLE_AER for all couples (left) and only for not diagonal models (right). .....	11
Figure 6: Average NUM_STABLE_AER for each original bracketing pair. ....	12
Figure 7: Histograms of the third and fourth moments of 100000 simulations simulations of a Gaussian noise generated with NLOOP = 100 samples. ....	12
Figure 8: Histograms of the third and fourth moments of the atmospheric path reflectance at 412 nm after atmospheric correction. ....	13
Figure 9: Histograms of AER_MIX for stable and unstable cases. ....	14
Figure 10: Left, histogram of BPAC_RATE when the original BPAC_ON = 0. Right, histogram of (NLOOP-BPAC_RATE) when the original BPAC_ON = 1. ....	15
Figure 11: Histograms of mean difference (left) and standard deviation (right) of marine reflectance at 412 nm. Top: stable aerosol models, middle: unstable aerosol models, bottom: all models.....	17
Figure 12: Histograms of mean difference (left) and standard deviation (right) of aerosol reflectance at 412 nm. Top: stable aerosol models, middle: unstable aerosol models, bottom: all models.....	18
Figure 13: Histograms of mean difference (left) and standard deviation (right) of path reflectance at 412 nm. Top: stable aerosol models, middle: unstable aerosol models, bottom: all models.....	19
Figure 14: Stable aerosols (left: all, right: couple (5,12)), standard deviation of $\rho_w$ for three water types.....	21
Figure 15: Unstable aerosols (left: all, right: couple (5,12)), standard deviation of $\rho_w$ for three water types.....	22
Figure 16: All aerosols (left: all, right: couple (5,12)), standard deviation of $\rho_w$ for three water types. ....	23
Figure 17: Stable aerosols, standard deviation of $\rho_w$ clear waters for six different pairs of bracketing aerosol models: (0,0), (0,4), (3,7), (4,8), all couples within the range (13,30) and (31,31) (Inherent Optical Properties model).....	24
Figure 18: Occurrence frequencies of (model 1, model 2) couples of aerosol models among a selection of 40 half-orbits. ....	25
Figure 19: Stable aerosols, all geometries. Six different pairs of diagonal bracketing aerosol models: (0,0), (2,2), (3,3), (8,8), (21,21), and (31,31). ....	28
Figure 20: Couple (0, 0), different geometries.....	29
Figure 21: Couple (31, 31), different geometries. ....	30
Figure 22: Stable aerosols, all geometries. Six different pairs of non-diagonal bracketing aerosol models: (0,4), (3,7), (4,8), (8,8), (9,31), and (18,15). ....	31
Figure 23: Couple (0, 4), different geometries.....	32
Figure 24: Couple (5, 12), different geometries.....	33
Figure 25: Couple (5, 12), not originally turbid (left) and originally turbid (right). Stable models (top) and all models (bottom). ....	34
Figure 26: Standard deviation of $\rho_w$ (normalized by $\rho_w$ ) for couple (4,8) and its median curve. ....	36
Figure 27: Left: percent amount of the steps of ppathstar / pR at 865 nm for which a couple was find. Right: amount of geometry configurations for each couple. ....	39
Figure 28: Relationships between Std( $\rho_{\text{pathstar}}$ ), Std(t), and Cov( $\rho_{\text{pathstar}}$ , t) and $T_{\text{aer}}$ at 412 nm obtained for the couple (4,8) at one geometry grid point ('10 0 5'). ....	39
Figure 29: Relative difference between the simulated and the calculated uncertainties std( $\rho_w$ ) as a function of $\rho_w$ for <b>stable</b> observations of <b>case 1</b> waters. Couples (0,4) and (3,7), 412 nm.....	41
Figure 30: Relative difference between the simulated and the calculated uncertainties std( $\rho_w$ ) as a function of $\rho_w$ for <b>stable</b> observations of <b>case 1</b> waters. Couples (4,8) and (5,12), 412 nm.....	42




	SENTINEL-3 OPTICAL PRODUCTS AND ALGORITHM DEFINITION  ERROR PROPAGATION IN THE ATMOSPHERE CORRECTION	REF: S3-L2-SD-01-C01-ACR-TN VERSION: 1.2 DATE: 30 SEPTEMBER 2010 PAGE IV
--	---	---

Figure 31: Relative difference between the simulated and the calculated uncertainties $\text{std}(\rho_w)$ as a function of $\rho_w$ for <b>stable</b> observations of <b>case 1</b> waters. Couples (4,8), 560 nm.....	43
Figure 32: Relative difference between the simulated and the calculated uncertainties $\text{std}(\rho_w)$ as a function of $\rho_w$ for <b>all</b> (stable + unstable) observations of <b>case 1</b> waters. Couples (0,4) and (3,7), 412 nm. ....	44
Figure 33: Relative difference between the simulated and the calculated uncertainties $\text{std}(\rho_w)$ as a function of $\rho_w$ for <b>all</b> (stable + unstable) observations of <b>case 1</b> waters. Couples (4,8) and (5,12), 412 nm. ....	45
Figure 34: Relative difference between the simulated and the calculated uncertainties $\text{std}(\rho_w)$ as a function of $\rho_w$ for <b>stable</b> observations of <b>turbid</b> waters. Couples (0,4) and (3,7), 412 nm. ....	46
Figure 35: Relative difference between the simulated and the calculated uncertainties $\text{std}(\rho_w)$ as a function of $\rho_w$ for <b>stable</b> observations of <b>turbid</b> waters. Couples (4,8) and (5,12), 412 nm. ....	47

## LIST OF TABLES

Table 1: Precise values of Fig. 2 (resp. left and right) only for aerosol models between 0 and 12 (%) (resp. top and bottom). ....	9
Table 2: Most frequent couples of bracketing aerosol models and their corresponding amount (in %) among the 40 half-orbits. ....	26

	<p>SENTINEL-3 OPTICAL PRODUCTS AND ALGORITHM DEFINITION</p> <p>ERROR PROPAGATION IN THE ATMOSPHERE CORRECTION</p>	<p>REF: S3-L2-SD-01-C01-ACR-TN VERSION: 1.2 DATE: 30 SEPTEMBER 2010 PAGE V</p>
--	---	--

	SENTINEL-3 OPTICAL PRODUCTS AND ALGORITHM DEFINITION  ERROR PROPAGATION IN THE ATMOSPHERE CORRECTION	REF: S3-L2-SD-01-C01-ACR-TN VERSION: 1.2 DATE: 30 SEPTEMBER 2010 PAGE 1
---	---	--

# 1 INTRODUCTION

## 1.1 Scope

Aerosols have a strong contribution to top-of-atmosphere (TOA) reflectances in both visible and near-infrared (NIR) parts of the electromagnetic spectrum analyzed by optical instruments like MERIS and OLCI. Their major contribution must be removed in the visible part of the spectrum in order to retrieve marine reflectances from which ocean color properties are determined.

In the NIR marine reflectances are negligible in most cases and aerosols properties can be retrieved in this part of the spectrum: TOA reflectances arise only from the interactions between radiation, gas molecules and aerosols. However, multiple-scattering occurs between radiation and aerosols and strongly depends on the type of these aerosols.

The method used by the data processing chain of OLCI to deal with this problem is the one of Antoine and Morel (1998): typical models of aerosols are archived in Look-Up Tables (LUT) and aerosols properties are retrieved in the NIR by proximity of the observation to aerosol reflectances in two wavelengths (775 and 865 nm). The aerosol properties are then extrapolated in the visible part of the spectrum where the aerosol reflectances can be removed from the TOA reflectances. Two models of aerosols are selected to enclose a final solution consisting of a mixture of the two bracketing models, therefore a 'mixing ratio' is defined as the proportion of one of the bracketing model.

## 1.2 Purpose

The objective of this study is to evaluate the error propagation in the atmospheric correction step of OLCI. The analysis is performed on simulated data, starting from MERIS TOA radiances which are noised within the Sentinel-3 OLCI SNR specification.

Statistics are derived, including a sensitivity analysis which evaluates the response of the atmospheric correction algorithm to noise in the input signals.

A method is proposed to build Look-Up Tables (LUTs) for the estimation of the output noise. These LUTs are build once and for all for one specific input noise. A direct comparison between the simulated data and the computation of noise using the LUTs will show that this method is reliable for a fast extraction of error estimates.

## 1.3 References

### 1.3.1 *Applicable Documents*


This document is in compliance with the following applicable documents:

REF	TITLE	DOCUMENT CODE	VERSION	DATE
AD-1				

### 1.3.2 *Reference Documents*

The following reference documents were taken into account in preparing this document:

REF	TITLE	DOCUMENT CODE	VERSION	DATE
RD-1				

	SENTINEL-3 OPTICAL PRODUCTS AND ALGORITHM DEFINITION  ERROR PROPAGATION IN THE ATMOSPHERE CORRECTION	REF: S3-L2-SD-01-C01-ACR-TN VERSION: 1.2 DATE: 30 SEPTEMBER 2010 PAGE 3
--	---	--

## 2 METHODOLOGY

### 2.1 MEGS data processing

Using ODESA (MEGS data processing from level 1 to level 2), the aerosol atmospheric correction module can be isolated from other data treatments.

Among physical quantities retrieved by this module we investigate:

- aerosol reflectances  $\rho_a$
- atmospheric path (rayleigh+aerosol) reflectances  $\rho_{\text{pathstar}}$
- marine reflectances  $\rho_w$  (or ' $\rho_{\text{surf}}$ ')

Other parameters are used to investigate subcategories of data pixels:

- aerosol bracketing models: the pair of aerosol models selected for the retrieval
- AER\_MIX: the aerosol mixing ratio
- BPAC\_ON: a flag identifying the Bright Pixel Atmospheric Correction (BPAC) treatment for turbid waters (water cases where NIR marine reflectances are no longer negligible)
- geometry (solar zenith angle, viewing zenith angle, difference in azimuth)

The latest version of MEGS implemented in ODESA allows the creation of breakpoints in NETCDF format, the physical quantities and the other parameters are exported via this interface after modifications in the raw code.

Inputs of the processing are level 1 data, they provide situations with various observing geometries, aerosol types and water types. When one specific kind of situation is to be investigated we collect a specific set of observations.

### 2.2 Implementing a noise loop in the data processing

The methodology can be summed up by the processing chart in Figure 1. In MEGS the aerosol atmospheric correction is called at some point of the processing and a noise loop is implemented inside the routine. It first processes the retrieval with the original TOA radiances. Then, it processes the retrieval with the noised radiances for which statistics are computed by comparison with the original solution.

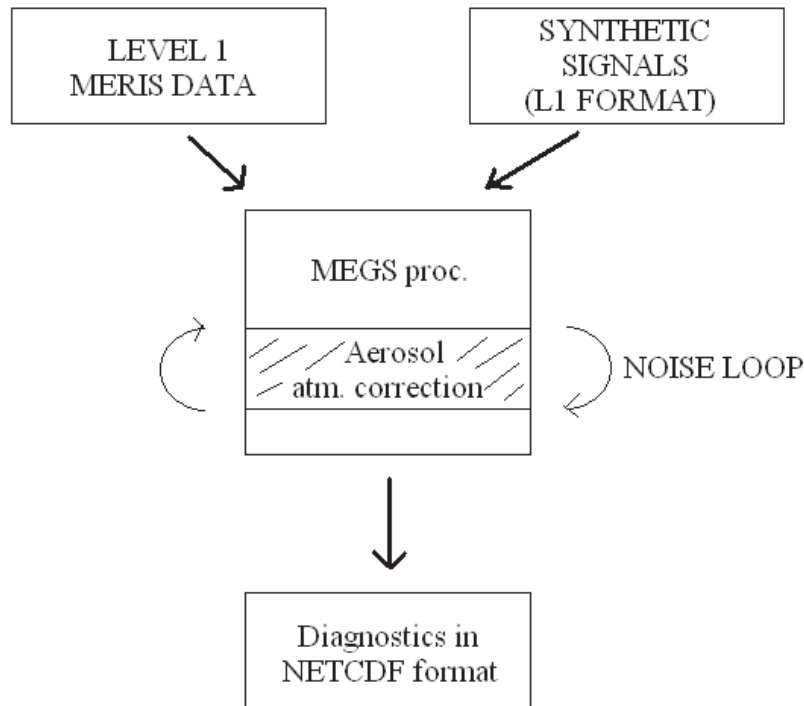


Figure 1: Processing chart of data processing through MEGS.

The noise loop consists in adding a Gaussian noise to the original TOA radiances measured by MERIS. These radiances are glint-corrected. The Gaussian noise is only applied to the two NIR wavelengths used for the determination of the aerosol properties (775 and 865 nm). To generate this noise we use the Box-Müller algorithm: two independent random variables are generated for the two wavelengths, each following a Gaussian statistics with mean 0 and standard deviation 1. Since the noise is discretized over loop steps a strong computational limitation is the amount of loop steps performed for each data pixel. We set this amount to NLOOP=100 as a compromise between computation time and gaussianity.


We use the Sentinel-3 SNR specification noise ('B02') over the NIR radiances. Input reflectances are converted into radiances, the noise is applied to the radiances and the radiances are finally converted back to reflectances.

The amplitude value 'VAL' of the Gaussian noise distribution depends on the TOA radiance L by:

- if  $L > L_0$  :  $VAL^2 = a.L + b.L^2$

- if  $L = L_0$  :  $VAL(L_0)^2 = a.L_0 + b.L_0^2$

- if  $L < L_0$  :  $VAL = VAL(L_0)$

	SENTINEL-3 OPTICAL PRODUCTS AND ALGORITHM DEFINITION  ERROR PROPAGATION IN THE ATMOSPHERE CORRECTION	REF: S3-L2-SD-01-C01-ACR-TN VERSION: 1.2 DATE: 30 SEPTEMBER 2010 PAGE 5
--	---	--

Where a and b are constants and  $L_0$  is a constant threshold radiance, they all depend on the wavelength.

For the two NIR wavelengths (resp. 775 and 865 nm) values a, b and  $L_0$  are (resp.):

$$a = 1.04466.10^{-5} \text{ and } 1.5962.10^{-5}$$

$$b = 2.0962.10^{-7} \text{ and } 2.28978.10^{-7}$$

$$L_0 = 0 \text{ and } 6.4 \text{ W.sr}^{-1}.\text{m}^{-2}.\text{nm}^{-1}$$

## 2.3 Scene selection

A first simulation of noise propagation is made over a level 1 half-orbit from MERIS observations (half-orbit '20051227\_035604'). For a detailed investigation we secondly use numerous observations provided by the processing of 40 half-orbits. These observations will be split into data corresponding to specific aerosol couples and geometries.

## 3 RESULTS OF A NOISE SIMULATION ON A SPECIFIC HALF-ORBIT

In this section we make noise simulations over data from one specific half-orbit ('20051227\_035604'). For this half-orbit the amount of pixel data is considerable (about 5 million pixels) and the computation takes a long time (about three days) because of the amount of noise loops performed over oceanic pixels. We only look at observations over ocean although all observations are recorded in the NETCDF output.

Analysis tools have been developed to automatize the selection of several possible variables (different reflectances, wavelengths, geometries,...). These tools use mexnc routines on matlab.

### 3.1 General statistics

One example application of these tools is a statistics of the couples of aerosol models selected in the atmospheric correction algorithm (in the original retrieval, that is to say without noise).

Figure 2 shows the percentage of couples (model 1, model 2) as they were retrieved along the first half-orbit. It is made separately when diagonal models (see below) are considered (left) or not (right).

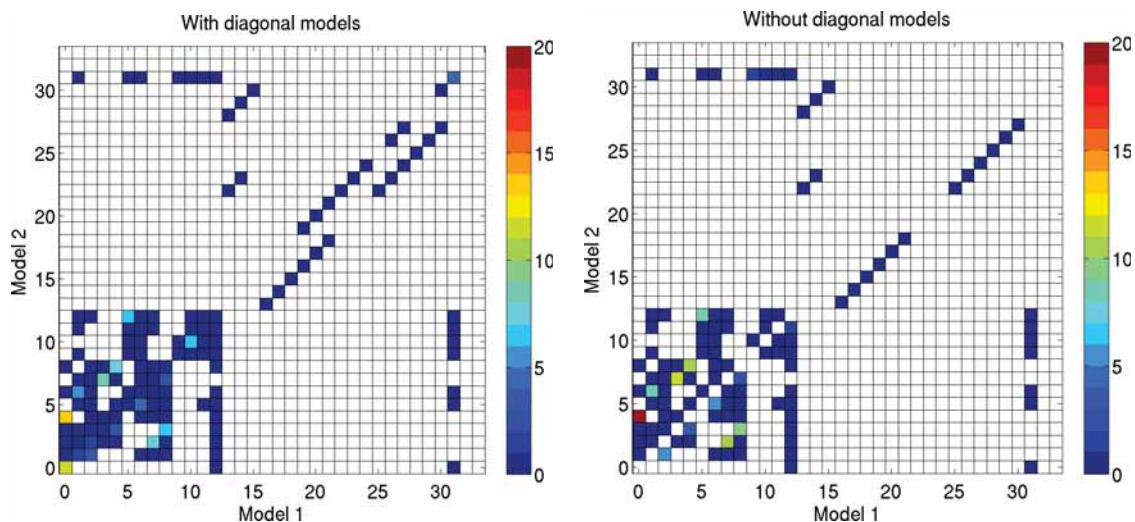



Figure 2: Occurrence frequencies of (model 1, model 2) couples of aerosol models along the half-orbit '20051227\_035604' (%). With (left) and without (right) diagonal models.

	SENTINEL-3 OPTICAL PRODUCTS AND ALGORITHM DEFINITION  ERROR PROPAGATION IN THE ATMOSPHERE CORRECTION	REF: S3-L2-SD-01-C01-ACR-TN VERSION: 1.2 DATE: 30 SEPTEMBER 2010 PAGE 7
---	---	--

The selection of the two bracketing aerosol models is made by the comparison between the observed ratio  $\rho_{\text{path}}(775) / \rho_R(775)$  (where  $\rho_R$  is the Rayleigh reflectance at 775 nm) and the ratio extrapolated from the observed ratio at 865 nm for each aerosol model. The selected bracketing models have ratios at 775 nm embracing the observed ratio  $\rho_{\text{path}}(775) / \rho_R(775)$ .

### 3.1.1 *Diagonal models*

It is sometimes possible that the observed ratio at 775 nm is excessively low or excessively high, in such cases the algorithm finds (resp.) only one lowermost or one uppermost model to select. Such ‘diagonal’ model is selected to form the bracketing couple (i.e. the couple consists in twice the same model) and the mixing ratio AER\_MIX is either set to 0 (no aerosol ratio at 775 nm higher than the observed ratio) or 1 (no aerosol ratio at 775 nm lower than the observed ratio).

In most diagonal cases the observed ratio is excessively low (AER\_MIX=1). The couple (0,0) is particularly occurrent because it is usually the ‘lowest’ aerosol model. It is not always the case as tests on absorbing aerosols sometimes reduce the model selection to absorbing models only. Also, other diagonal couples are found in regions bordering glint or in presence of thin cirrus as an effect of radiance contamination. When such situation occurs flags are raised in MEGS. These flags were not taken into account in the presented statistics.

As a matter of fact, the extrapolated ratio at 775 nm of the selected diagonal model is generally far from the observed  $\rho_{\text{path}}(775) / \rho_R(775)$  ratio compared to the distance between the ratios for the two embracing models when these models are distinct. Figure 3 shows the difference  $(\text{aer-obs})/\text{obs} \times 100 \%$  of the extrapolated ratio relatively to the observed one for the diagonal model 0 (left) and for other diagonal models (middle) as well as the difference  $(\text{aer2-aer1})/\text{obs} \times 100 \%$  between the extrapolated ratios of the embracing models when these models are distinct (right). Please note that the latter is only shown for the comparison of the order of magnitude, by definition of the mixing ratio AER\_MIX there is no difference  $(\text{aer-obs})/\text{obs}$  in the case of distinct models.

For the diagonal model (0,0) the difference is always positive (the very few negative values are not shown) as the selection of this model is mostly made when there is no ‘lower’ aerosol model. The other diagonal models can show positive or negative differences as, sometimes, absorbing or inherent optical properties (IOP) models are used exclusively and the lowest model is not 0.

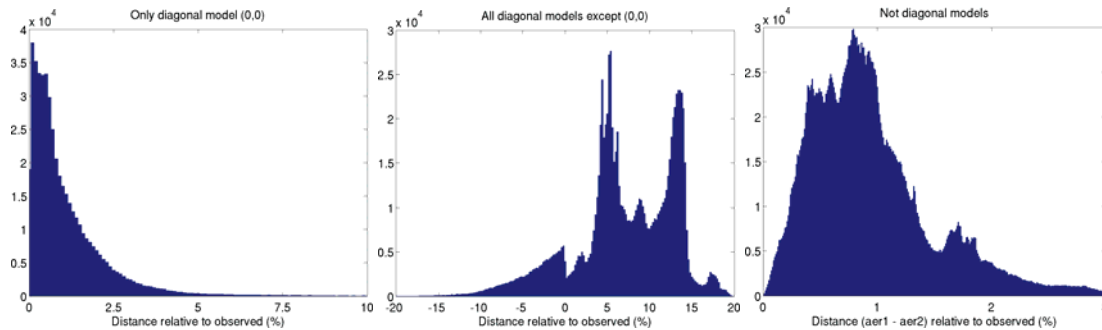


Figure 3: Relative differences between extrapolated and observed ratio at 775 nm for diagonal model 0 (left) and all other diagonal couples (middle). Relative difference of the bracketing aerosol ratio relatively to the observed ratio for non-diagonal couples (right).

The main difference is in the order of magnitude: while the extrapolated ratio from model 0 stays relatively close to the observed ratio (as compared to the Figure 3, right) the other diagonal models can reach large differences (up to 20 %). **Retrievals including diagonal models should therefore not be considered valid for further use, all the more when the model is not 0. We will however present some results including diagonal models to show the behaviour of these cases.**

### 3.1.2 General considerations

For aerosol models between 0 and 12 the occurrence values seen in Figure 2 (resp. left and right) are more precisely shown in Table 1 (resp. top and bottom, values smaller than 0.01 are left to 0.00). Some aerosol couples are very seldom or never represented.

The amount of couples with both aerosol models between 13 and 30 is 0.46 % (resp. 0.57 % without diagonal models).

The amount of couples including at least one model 31 (IOP model) is 5.50 % (resp. 1.39 %).

These statistics are dependent on the observed orbit but qualitatively stable with regard to the most occurrent couples.

With diagonal couples

12		0.00	0.00			6.20	0.01	0.01			0.00	0.00	0.52
11		0.00				0.02	0.00	0.00		0.00	0.00	0.56	0.85
10						0.01	0.00			0.00	6.06	0.51	0.00
9		0.00				0.00	0.00			2.74	0.00	0.00	0.00
8	0.00		0.00	0.41	7.36		0.00	0.00	0.01				0.00
7		0.00	0.01	3.27	0.00		0.00	0.06	2.08				
6	0.00	5.96	0.04			0.00	0.00	0.00	0.00				0.00
5		0.03	0.00		0.00	0.31	4.17	0.00	0.00			0.00	0.01
4	13.92		0.00	0.00	0.02		0.00	0.00	0.00				0.00
3	0.02	0.00	0.00	0.42	2.37				0.01				0.00
2	0.00	0.00	1.38	0.05	0.00			7.33	0.02				0.00
1	0.00	1.45	3.51				0.01	0.05	0.00				0.00
0	11.05												0.02
2 ↑ 1 →	0	1	2	3	4	5	6	7	8	9	10	11	12

Without diagonal couples

12		0.01	0.00			3.53	0.01	0.01			0.00	0.00	
11		0.00				0.01	0.00	0.00			0.00		1.19
10						0.01	0.00			0.00		0.72	0.00
9		0.00				0.00	0.00				0.05	0.00	0.00
8	0.00		0.00	0.57	10.17		0.00	0.00					0.00
7		0.00	0.01	11.44	0.00		0.00		2.35				
6	0.00	2.25	0.03			0.00		0.00	0.00				0.00
5		0.04	0.00		0.00		5.76	0.00	0.00			0.00	0.01
4	10.32		0.00	0.00			0.00	0.00	0.00				0.00
3	0.04	0.00	0.00		3.30				2.12				0.00
2	0.00	0.00		0.07	0.00			10.37	0.05				0.00
1	0.00		5.27				0.01	0.07	0.00				0.00
0													0.04
2 ↑ 1 →	0	1	2	3	4	5	6	7	8	9	10	11	12

Table 1: Precise values of Fig. 2 (resp. left and right) only for aerosol models between 0 and 12 (%) (resp. top and bottom).

When simulating noise over input radiances the selection of models may be affected and the BPAC\_ON flag may be turned on/off when it is originally on or off. Therefore, we must consider these effects statistically for each data pixel.

The differences between the noised retrievals and the original retrieval are firstly assessed with the quantities described in Figure 4.

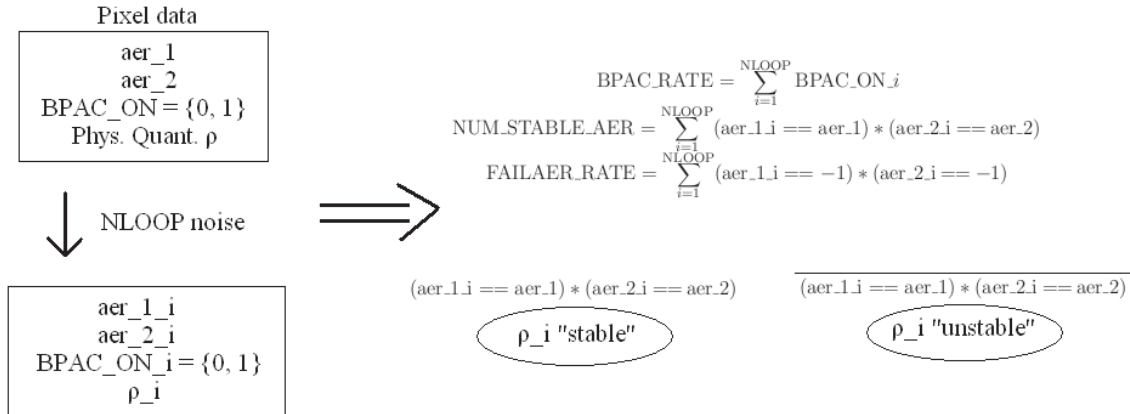


Figure 4: Statistical quantities derived from a noise loop over one pixel data.

FAILAER\_RATE is the amount of invalid retrievals (aerosol models set to the 'invalid couple' (-1, -1) ) if the original retrieval is good. For the selected half-orbit only very few retrievals are found having a positive amount of invalid retrievals if the original retrieval is good (0.009 %). We do not use these data pixels.

NUM\_STABLE\_AER is the amount of stable couples of aerosol models. The addition of noise may lead to a change in the selected pair of bracketing aerosol models as a consequence of changes in the ratios  $\rho_{\text{path}}(865) / \rho_R(865)$  and  $\rho_{\text{path}}(775) / \rho_R(775)$ . Among NLOOP loop steps NUM\_STABLE\_AER data pixels have the same pair of models as the original retrieval, in these cases the couple is said 'stable'. It is 'unstable' otherwise. Figure 5 shows a histogram of NUM\_STABLE\_AER for all couples (left) and only for not diagonal couples (right). The couple is usually stable although each noise simulation brings a mixture of stable and unstable cases. 30 % of the cases have no deviation from the original selected couple (about 10 % among not diagonal couples). Diagonal couples are more stable because the distance between the observed and the extrapolated ratios is larger, thus not diagonal couples have a more spreaded statistics and a lower peak on Figure 5, right.

As the original solution is firstly retrieved the stability is evaluated at each loop steps and statistics of reflectances are assessed separately among stable and unstable models. Statistics for the 'all' case (no distinction between stable and unstable models) is deduced from both statistics.

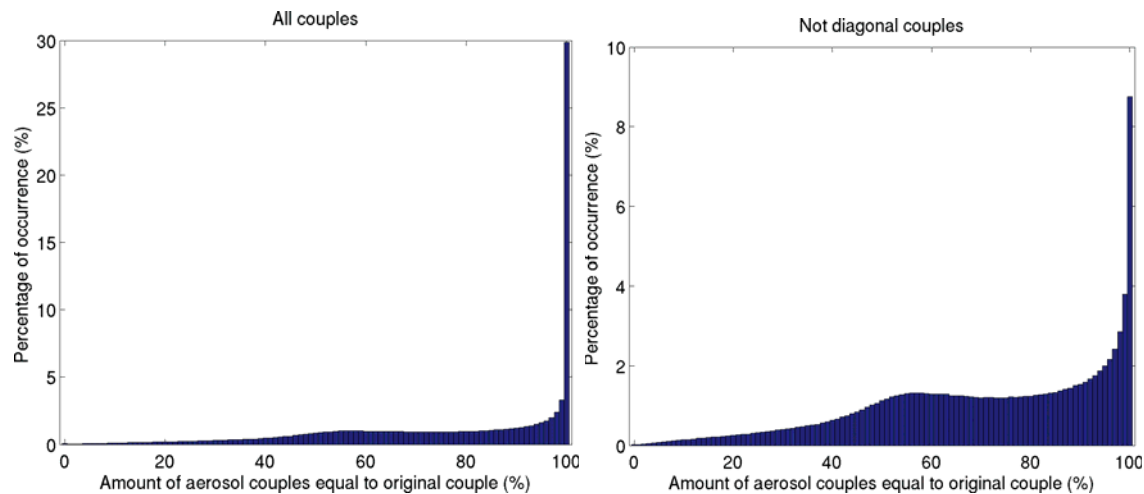


Figure 5: Histogram of NUM\_STABLE\_AER for all couples (left) and only for not diagonal models (right).

Following Figure 2 (left) an average NUM\_STABLE\_AER is computed for each pair of bracketing aerosol models in Figure 6. The diagonal couples are very stable as a consequence of the distance between observed and extrapolated  $\rho_{\text{path}}(775) / \rho_{\text{R}}(775)$  when a diagonal model is selected.

When processing the noise loop it is likely that stable and unstable cases correspond to specific values of the noised input radiances. Because the noise is Gaussian, instability may rather be reached for extreme values of the noise profile. This possibly impacts the gaussianity of the output reflectances (and of the other parameters) at other wavelengths than the NIR and when considering stable, unstable or all cases.

To discuss this point we separate cases into very stable cases (NUM\_STABLE\_AER > 90 %), very unstable cases (NUM\_STABLE\_AER < 50 %) and all cases (no distinction). gaussianity of (for example) the atmospheric path reflectance at 412 nm is examined by means of the third and fourth order moments of the standard normal distribution for each pixel. These moments must ideally be 0 and 3 respectively. However, the use of a small amount of loop steps (NLOOP = 100) makes the computation of the moments only 'relatively close' to 0 and 3. To highlight this fact Figure 7 shows distributions of the third and fourth order moments obtained from 100000 simulations of a Gaussian noise generated with NLOOP = 100 samples.

We see the third and fourth order moments are not strictly 0 and 3 because of the relatively small amount of samples. Using more samples increases computation time drastically and is not viable for our sensitivity analysis.

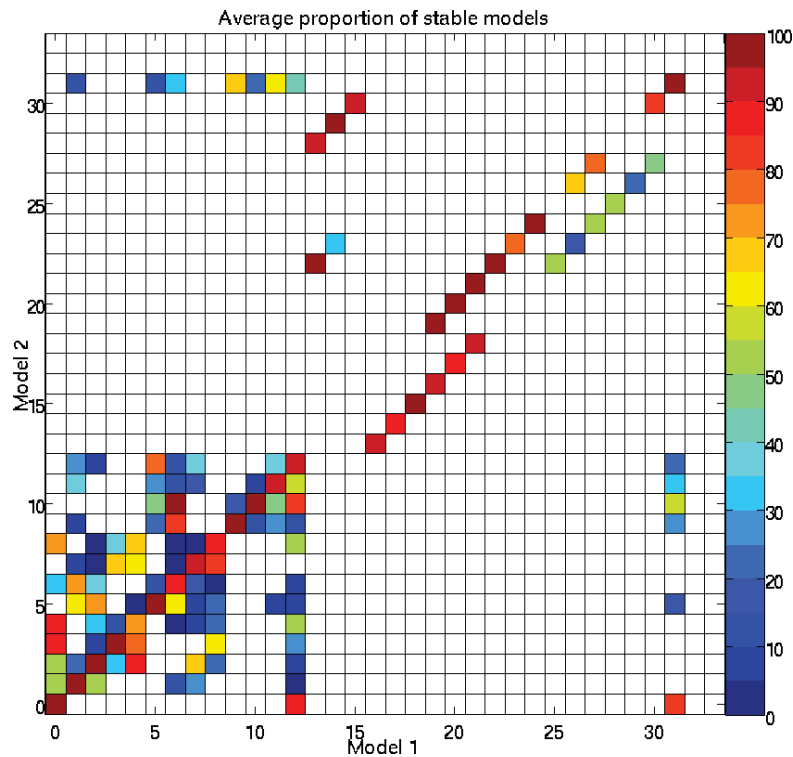


Figure 6: Average NUM\_STABLE\_AER for each original bracketing pair.

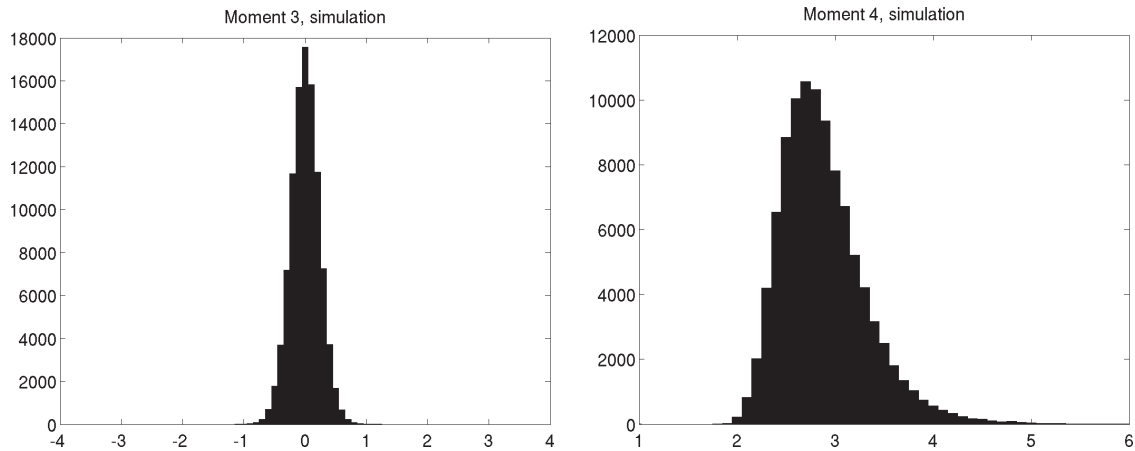


Figure 7: Histograms of the third and fourth moments of 100000 simulations of Gaussian noise generated with NLOOP = 100 samples.

Figure 8 now compares the third and fourth order moments obtained from about 100000 atmospheric path reflectances (i.e. 100000 pixels, one third and one fourth moments for each pixel) at 412 nm and separating very stable, very unstable and all cases.

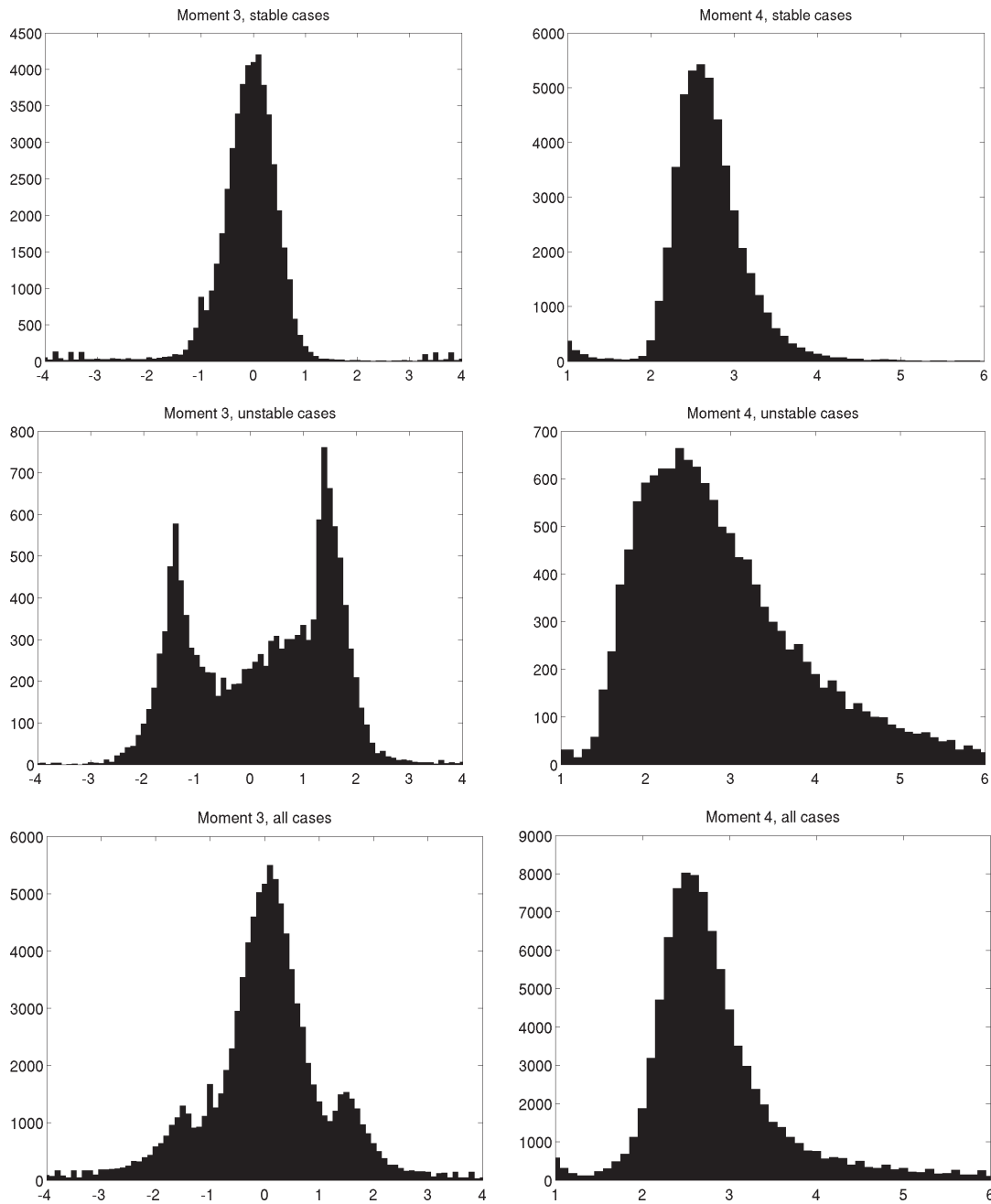


Figure 8: Histograms of the third and fourth moments of the atmospheric path reflectance at 412 nm after atmospheric correction.

Adding Gaussian noise to the input radiances at 775 and 865 nm leads to relatively Gaussian statistics in the output path reflectances at 412 nm. This means that Gaussian statistics of the atmospheric correction outputs can be performed for each pixel. This is true for the stable cases but untrue for the unstable cases (third moment way out of 0) as the change in aerosol models induce a different departure from the original output.

It can be shown that all physical parameters other than the atmospheric path reflectance perform identically.

In the global statistics unstable cases do not occur very often (see again Figure 5) and then have a small impact overall.

When no noise is applied it would be useful to predict whether a pixel is sensitive to instability or not. On this purpose Figure 9 shows the distribution of AER\_MIX for the same unstable and stable categories as used for Figure 8.

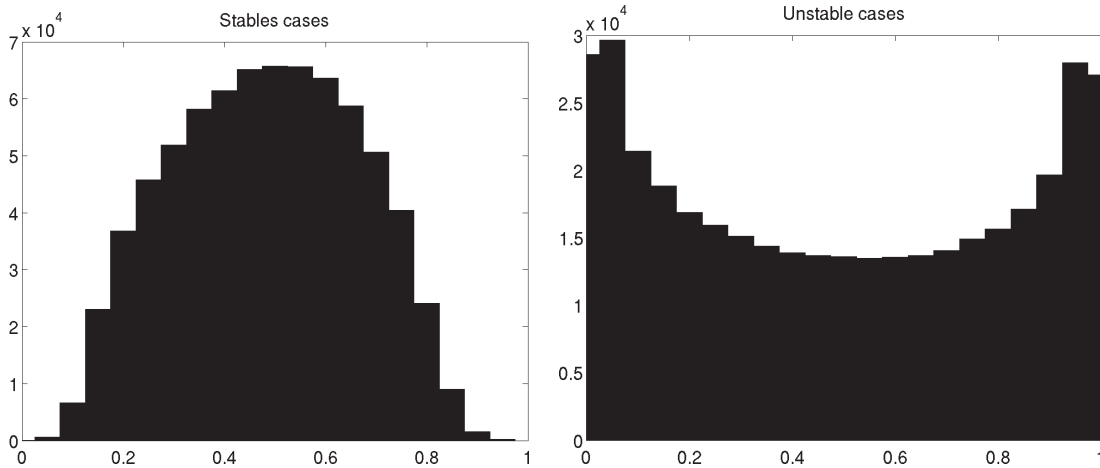


Figure 9: Histograms of AER\_MIX for stable and unstable cases.

It appears that most stable cases have a mixing ratio around 0.5 while unstable cases exhibit more extreme values (ratios closer to 0 or 1). However, the separation between the two classes is not strict and a mixing ratio close to 0.5 only means that the case is more likely to be stable. **Therefore, it is difficult to assess instability only from AER\_MIX.** Other influences such as the noise amplitude should be investigated because the noise amplitude is an increasing function of radiances.

BPAC\_RATE is the amount of loop steps for which turbid waters are detected (BPAC\_ON = 1): adding noise may lead to consider turbid waters while the observed situation is originally detected as clear (BPAC\_ON = 0). It may also lead to consider case 1 waters while the observed situation is originally detected as turbid (BPAC\_ON = 1). Figure 10 shows (left) a histogram of the occurrence of BPAC\_RATE when BPAC\_ON = 0 and (right) a histogram of NLOOP-BPAC\_RATE when BPAC\_ON = 1 (clear cases when originally turbid).

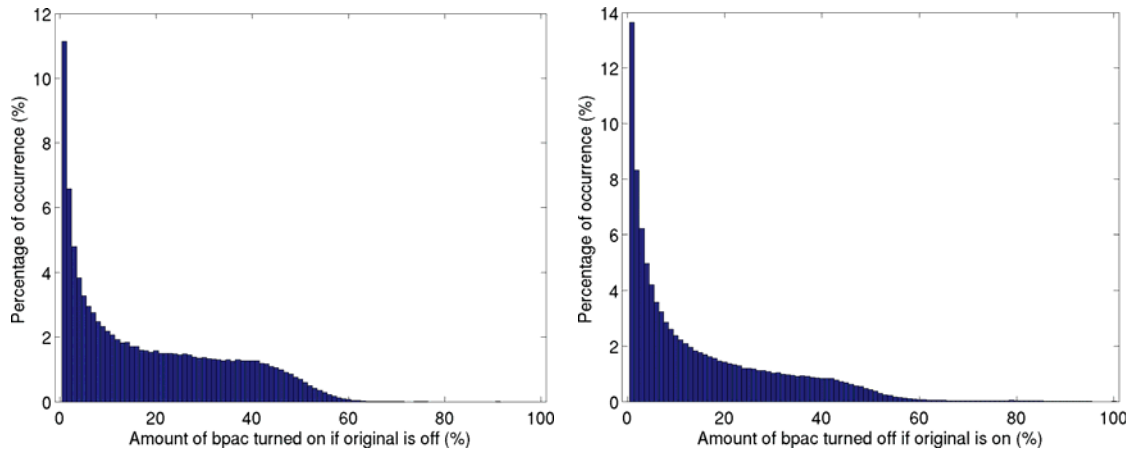


Figure 10: Left, histogram of BPAC\_RATE when the original BPAC\_ON = 0. Right, histogram of (NLOOP-BPAC\_RATE) when the original BPAC\_ON = 1.

### 3.2 Statistics on reflectances at 412 nm

Statistics on reflectances at 412 nm are performed separately for stable, unstable, and all aerosols (stable + unstable cases). Each MERIS observation with original reflectance  $\rho_0$  (say for example marine reflectance) provides a mean difference  $\Delta\rho$  and a standard deviation (assuming the mean is the original reflectance)  $\sigma_\rho$  for stable, unstable and all aerosols by


$$\Delta\rho = \frac{1}{N} \sum_{i=1}^N \rho_i - \rho_0$$

$$\sigma_\rho = \sqrt{\frac{1}{N} \sum_{i=1}^N (\rho_i - \rho_0)^2}$$

Both mean difference and standard deviation are expressed as percent of the original reflectance  $\rho_0$ .

As Figure 5 suggests, observations are usually stable with regard to the couple of bracketing aerosol models. Unstable cases are observed in a lesser extent. For the stable and unstable classes we must however ensure gaussianity. As a compromise we only use data pixels having a statistics of more than 50 % of NLOOP for a given category. That is to say NUM\_STABLE\_AER > 50 % NLOOP when considering stable aerosols and NLOOP - NUM\_STABLE\_AER > 50 % NLOOP when considering unstable aerosols. This leads to consider a total of 3955422 observations of stable cases (about 86 %) but only 632567 observations of unstable cases (about 14 %) among the half-orbit '20051227\_035604'. For the 'all' case the statistics is always NLOOP per data pixel.

In the following we show two-dimensional histograms of  $\Delta\rho$  (left) and  $\sigma_\rho$  (right) for marine, aerosol and path reflectances at 412 nm normalized by the original reflectance  $\rho_0$ . The color scale refers to

	SENTINEL-3 OPTICAL PRODUCTS AND ALGORITHM DEFINITION  ERROR PROPAGATION IN THE ATMOSPHERE CORRECTION	REF: S3-L2-SD-01-C01-ACR-TN VERSION: 1.2 DATE: 30 SEPTEMBER 2010 PAGE 16
---	---	---

probabilities normalized by the maximum probability for each interval of  $\rho_0$ : red colors code for high probabilities, blue colors code for low probabilities.

Results are shown for stable (top), unstable (middle) and all (bottom) aerosols.

The mean differences  $\Delta\rho$  are around zero which means that no bias is induced by propagating Gaussian noise. However, possible complex behaviors may appear (e.g. for  $\rho_{aer}$  in the case of unstable aerosol models) which most probably result from the fact that instability with regard to the pair of bracketing aerosol models is more likely to happen over a specific range of noise (for example on one tail of one of the Gaussian noise profile). On that matter the ‘all’ cases affirm more firmly that no bias is induced.

The standard deviations  $\sigma_\rho$  highlight more the impact of the error propagation with increasing uncertainty for decreasing reflectances. It is interesting to note different ‘modes’ (e.g.  $\rho_w$ ) which highlight the influence of different aerosol types, geometries and instability with regard to the turbid waters correction algorithm.

To investigate it further we develop the case of standard deviations of  $\rho_w$  for distinct water types and aerosol couples.

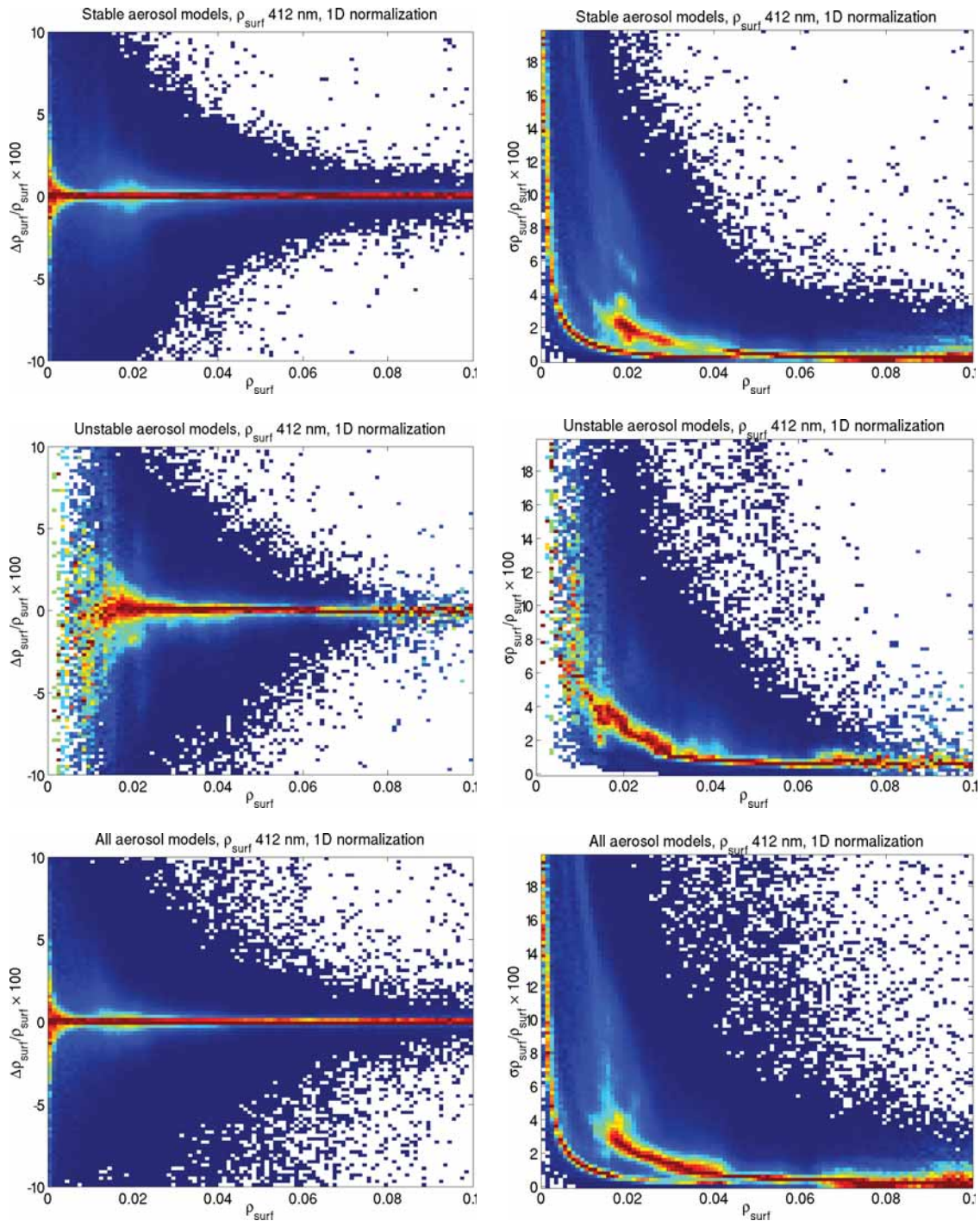


Figure 11: Histograms of mean difference (left) and standard deviation (right) of marine reflectance at 412 nm. Top: stable aerosol models, middle: unstable aerosol models, bottom: all models.

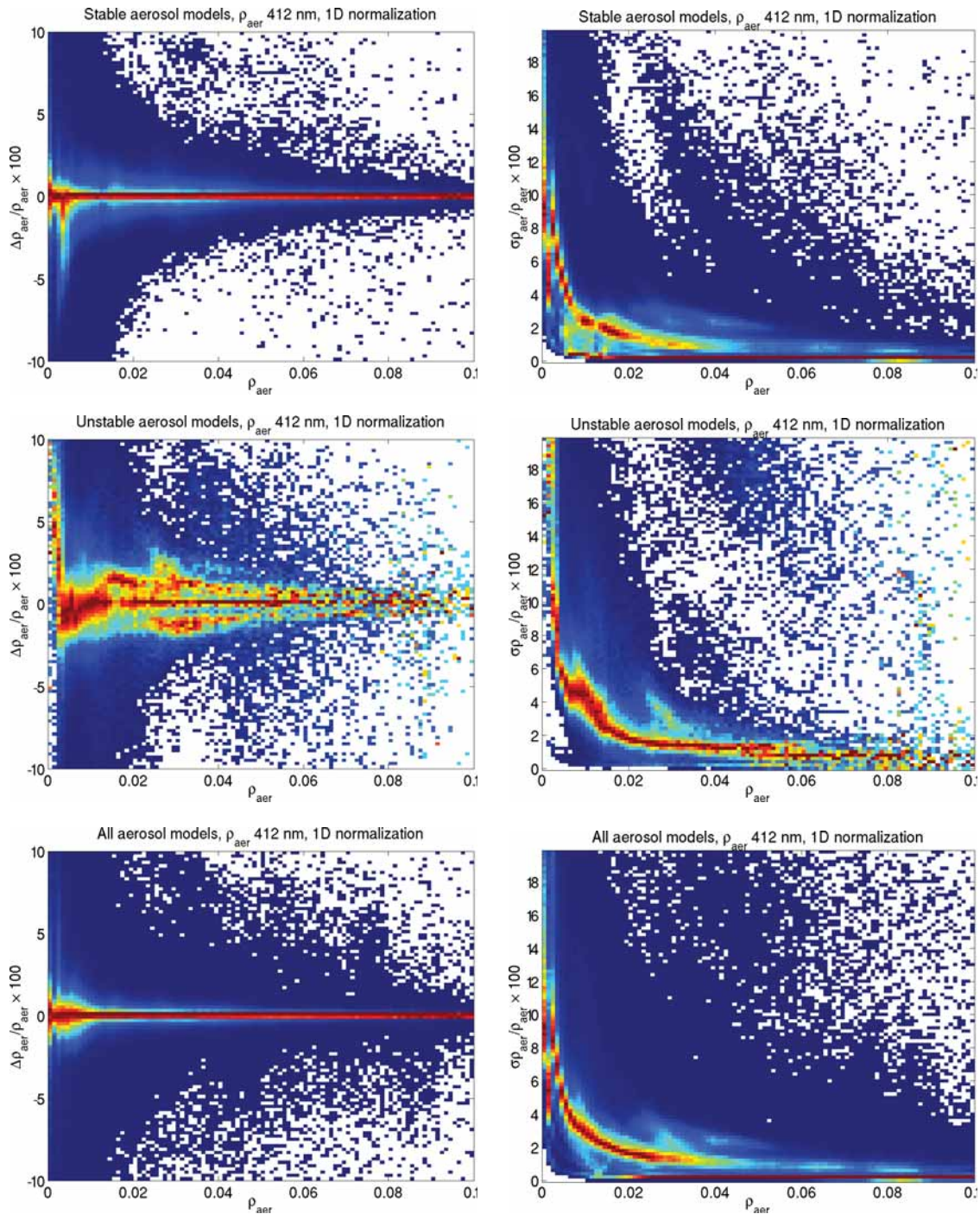


Figure 12: Histograms of mean difference (left) and standard deviation (right) of aerosol reflectance at 412 nm. Top: stable aerosol models, middle: unstable aerosol models, bottom: all models.

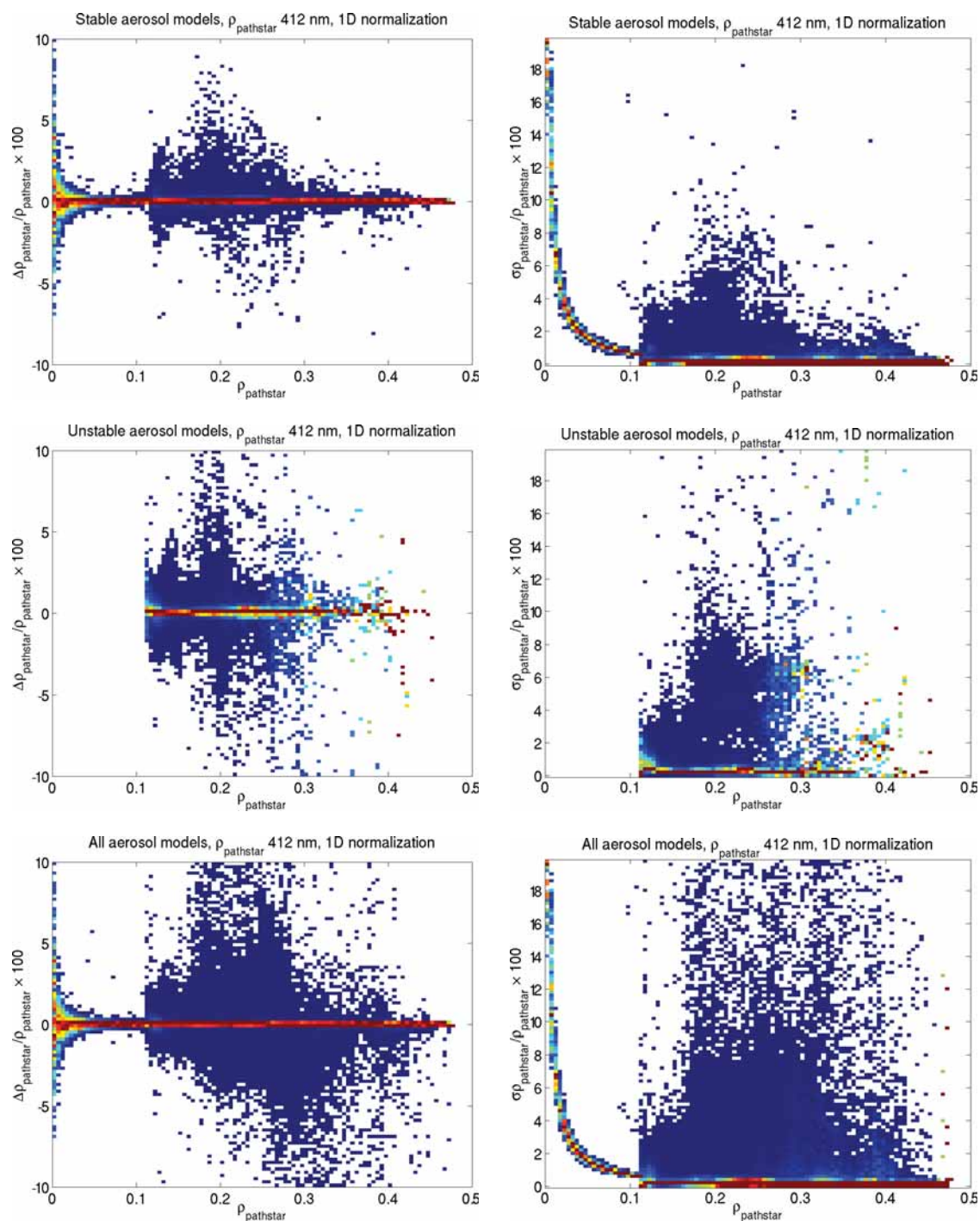



Figure 13: Histograms of mean difference (left) and standard deviation (right) of path reflectance at 412 nm. Top: stable aerosol models, middle: unstable aerosol models, bottom: all models.

	SENTINEL-3 OPTICAL PRODUCTS AND ALGORITHM DEFINITION  ERROR PROPAGATION IN THE ATMOSPHERE CORRECTION	REF: S3-L2-SD-01-C01-ACR-TN VERSION: 1.2 DATE: 30 SEPTEMBER 2010 PAGE 20
---	---	---

### 3.3 Statistics on marine reflectances $\rho_w$ at 412 nm for distinct water types and aerosol couples

We divide the  $\rho_w$  statistics into three water types as implied by selections of BPAC\_ON and BPAC\_RATE:

-clear waters: BPAC\_ON = 0 and BPAC\_RATE = 0, is the best case, no turbid water correction was performed

-sensitive waters: BPAC\_ON = 0 and BPAC\_RATE > 0, the original observation is sensitive to turbid correction

-turbid waters: BPAC\_ON = 1 and BPAC\_RATE > 0, the original observation is a case of turbid water

Figure 14, Figure 15 and Figure 16 show (resp.) the histograms of the standard deviation of  $\rho_w$  at 412 nm for the three water types for (resp.) the stable aerosols, the unstable aerosols, and for all aerosols (stable + unstable).

The results are shown for all couples of bracketing models (left) as well as for the couple (5,12) (right) which is the only pair of aerosol models having sufficient statistics (for each of the three water types) to allow the determination of these histograms for only one specific pair.

For all couples (left figures) clear waters show smaller standard deviations than sensitive and turbid waters. In one hand it is expected that turbid corrections enhance noise propagation. On the other hand, it is also possible that the difference observed between the three water types is induced by having different proportions of the different pairs of aerosol models in the statistics. For the argumentation Fig. 16 shows the standard deviation of  $\rho_w$  for clear waters only but separately for six different couples. It is clear that all couples do not necessarily exhibit the same profile.

The couple (5,12) contributes to a much higher proportion of the global statistics in sensitive and turbid waters (resp. 22.5 and 33.8 %) than in clear waters (0.7%). For the couple (5,12) (right figures) the standard deviations are only slightly smaller (in a comparison range of  $\rho_w$  between 0.01 and 0.02) for clear waters than for sensitive and turbid waters. Not regarding other possible influences (such as the viewing geometry) these results are the closest examples showing only a slight increase of the uncertainties in presence of turbid waters.

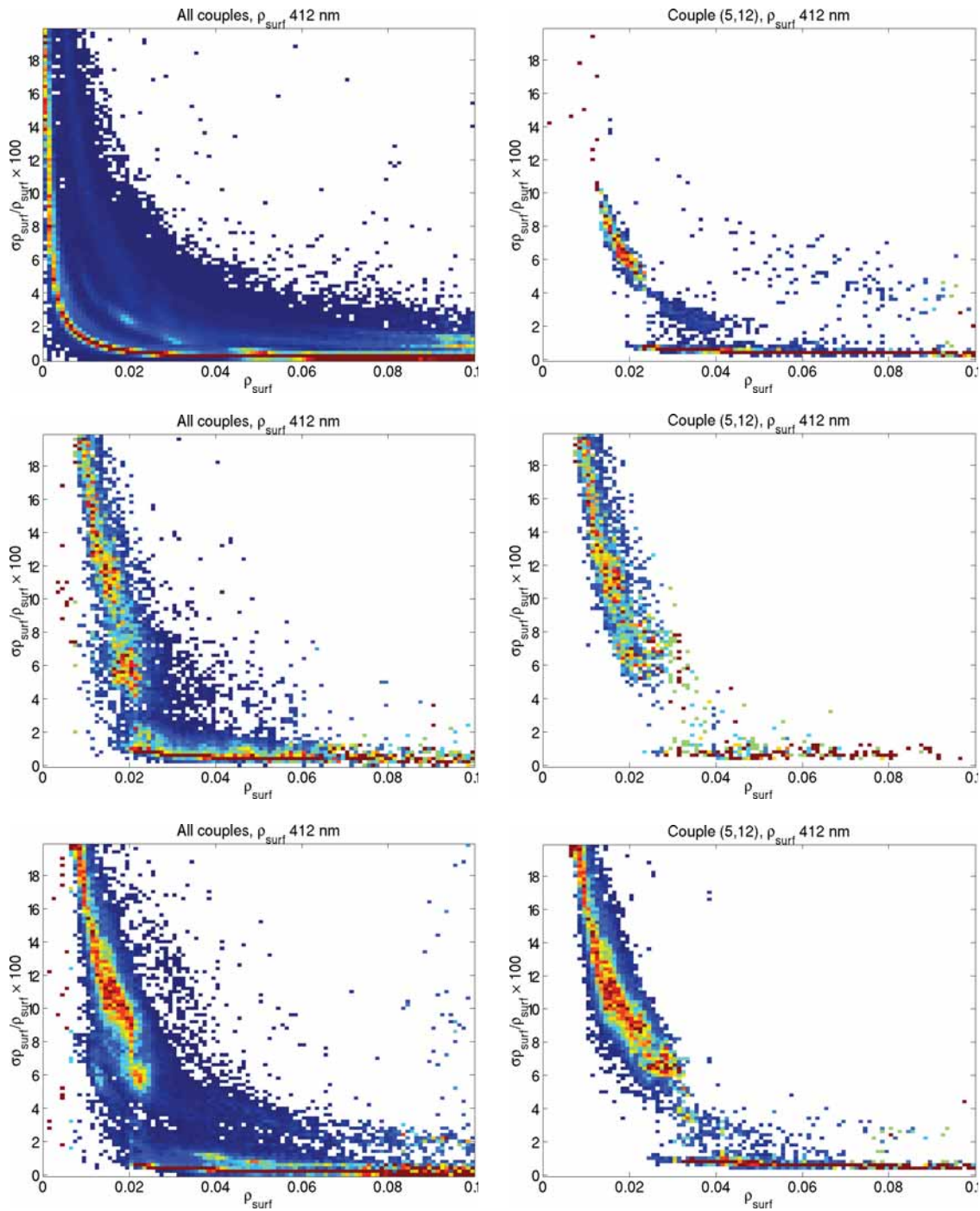


Figure 14: Stable aerosols (left: all, right: couple (5,12)), standard deviation of  $\rho_w$  for three water types.

Top: clear waters, middle: sensitive, bottom: turbid.

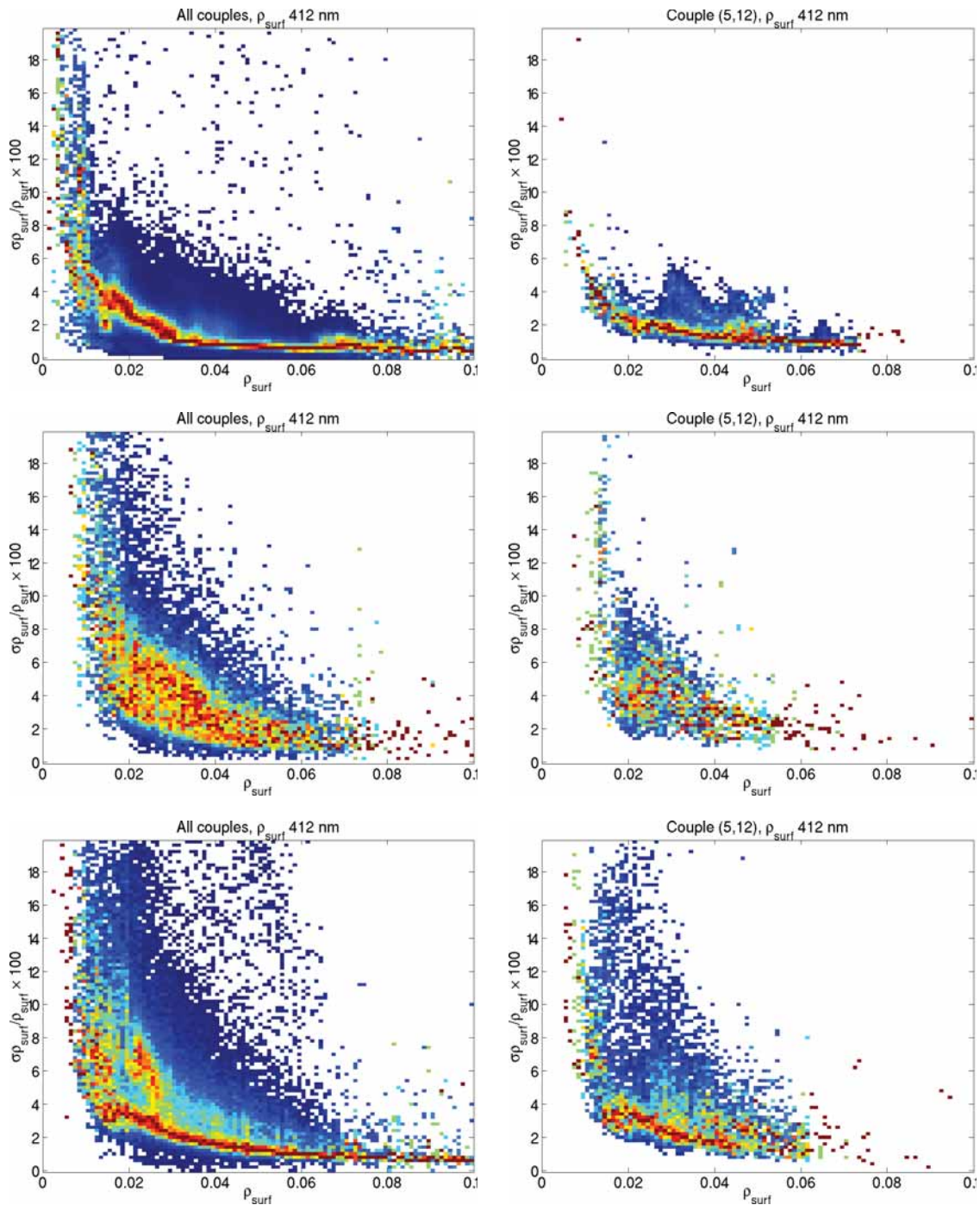


Figure 15: Unstable aerosols (left: all, right: couple (5,12)), standard deviation of  $\rho_w$  for three water types.

Top: clear waters, middle: sensitive, bottom: turbid.

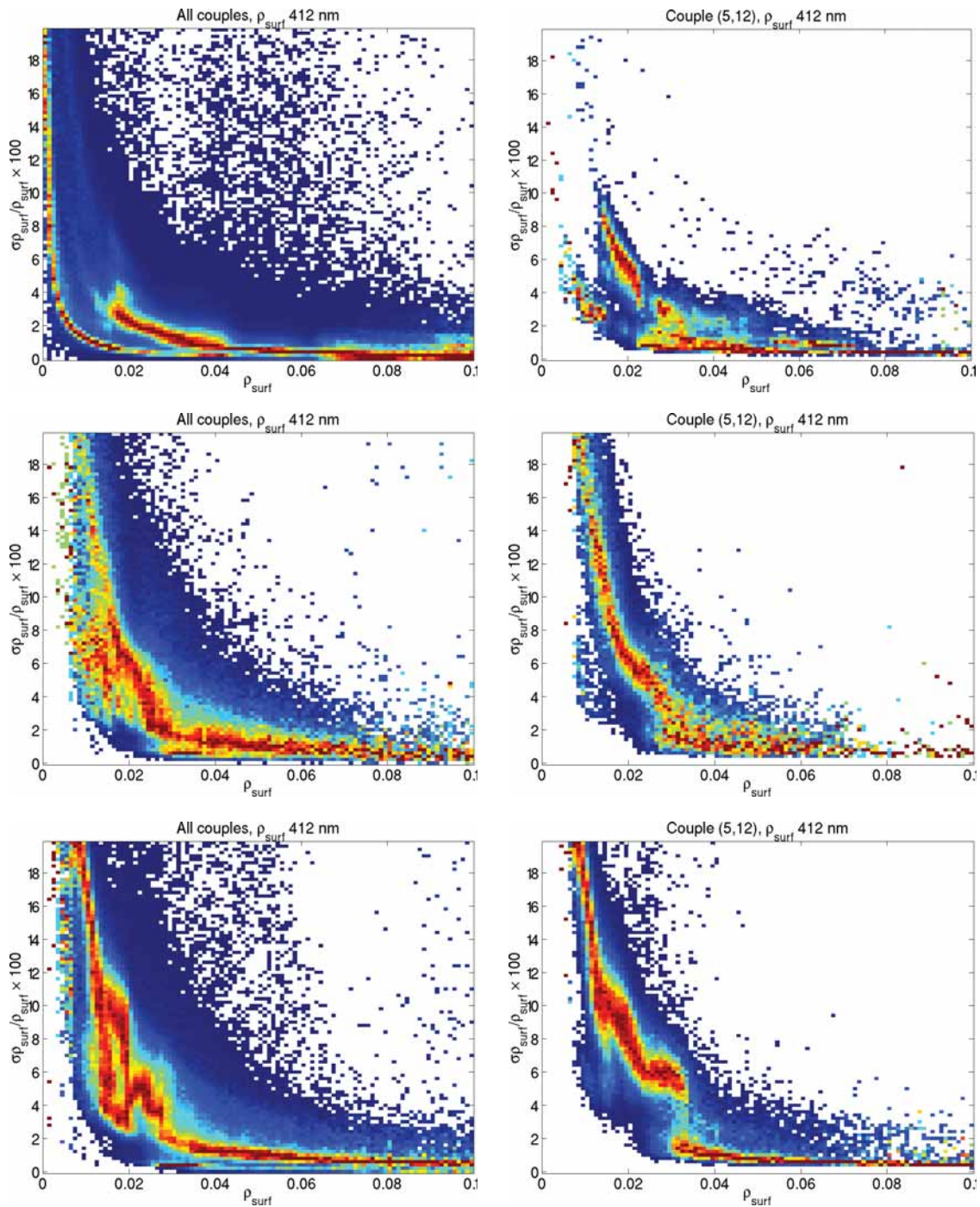


Figure 16: All aerosols (left: all, right: couple (5,12)), standard deviation of  $\rho_w$  for three water types.

Top: clear waters, middle: sensitive, bottom: turbid.

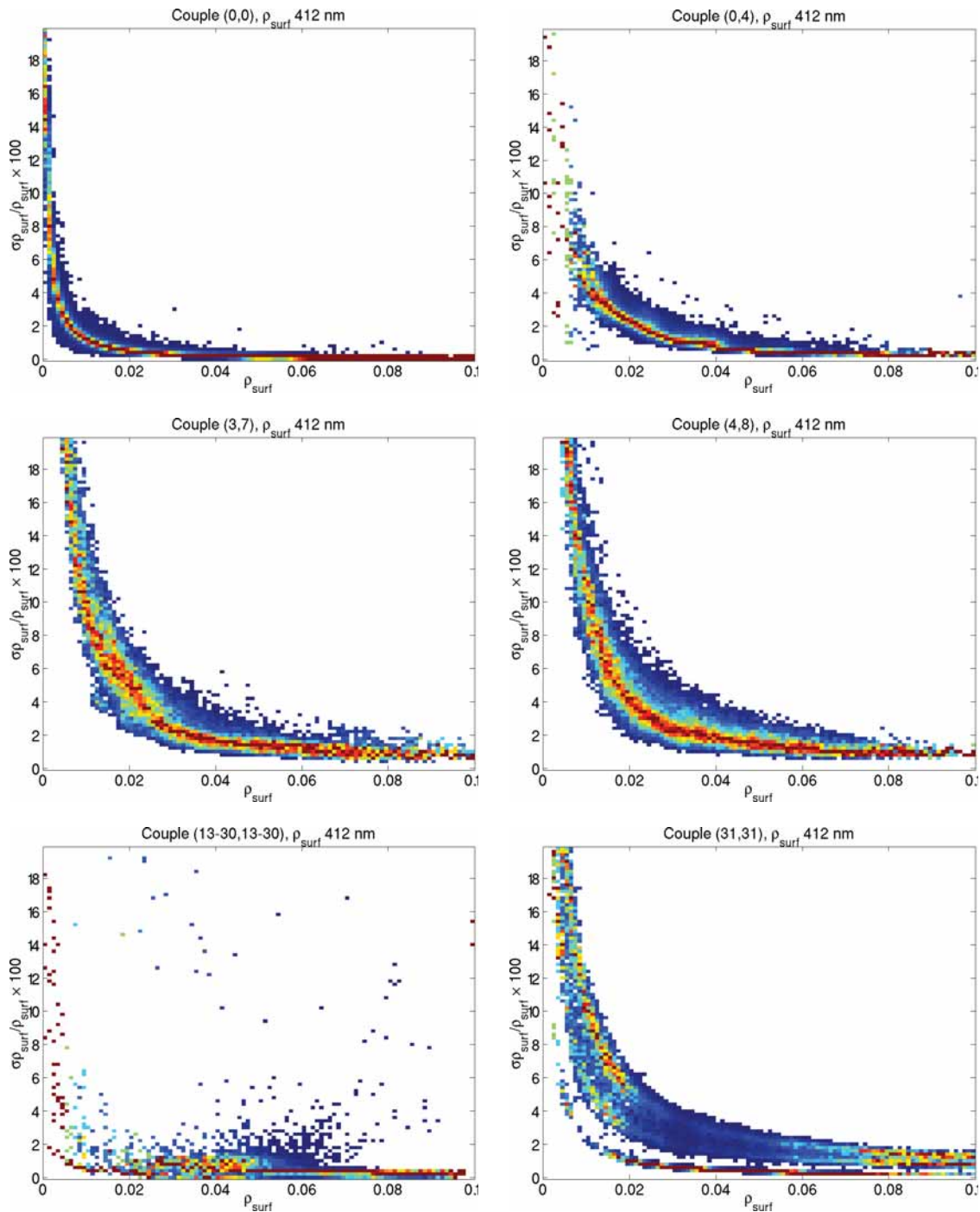


Figure 17: Stable aerosols, standard deviation of  $\rho_w$  clear waters for six different pairs of bracketing aerosol models: (0,0), (0,4), (3,7), (4,8), all couples within the range (13,30) and (31,31) (Inherent Optical Properties model).

## 4 NOISE SIMULATION ON 40 HALF-ORBITS, STATISTICS FOR DIFFERENT GEOMETRIES

To investigate a wider panel of cases 40 half-orbits have been processed on a computer cluster. For the best temporal and global sampling possible the first ten half-orbits of January, April, July, and September 2006 have been selected. After processing, data groups are made from all NETCDF outputs, they separate data pixels by couples of bracketing aerosol models.

We consider all types of waters and stable aerosols with NUM\_STABLE\_AER = NLOOP.

### 4.1 General statistics

As in Figure 2 occurrence frequencies of the couples of bracketing models can be computed, Figure 18 shows these frequencies for the 40 half-orbits.

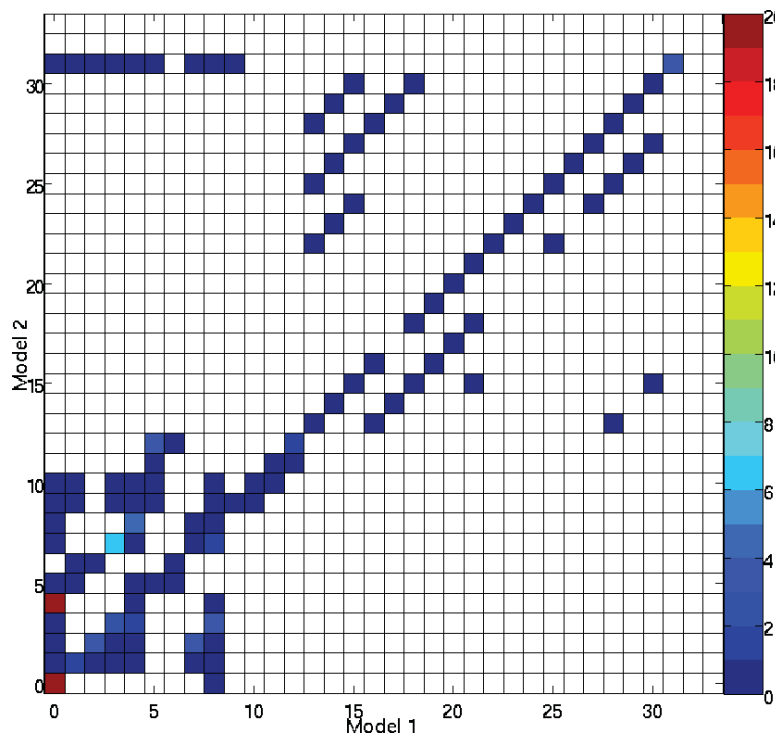


Figure 18: Occurrence frequencies of (model 1, model 2) couples of aerosol models among a selection of 40 half-orbits.

Among the 40 half-orbits many couples do not occur. However, some couples represented in Figure 2 are not represented in Figure 18 (for example many couples involving aerosol 1 model number 12).

**We cannot conclude that some couples are never used in the data processing. Rather, it is clear that some couples are much more used than others**, either from Figure 2 or from Figure 18. Table 2 sorts out all couples representing more than 0.1% of the statistics from the 40 half-orbits.

Model 1	Model 2	% of the statistics	Model 1	Model 2	% of the statistics
0	0	28.7	0	4	27.9
3	7	6.6	4	8	4.2
7	2	4.0	31	31	4.0
5	12	3.5	2	2	3.4
8	3	3.3	3	3	2.7
8	7	1.4	1	1	1.3
4	3	1.1	12	12	1.0
18	15	0.8	13	28	0.8
1	6	0.7	15	30	0.6
7	7	0.6	9	31	0.5
12	11	0.5	2	1	0.4
8	8	0.4	11	10	0.3
6	5	0.2	21	21	0.2
21	18	0.1	24	24	0.1

Table 2: Most frequent couples of bracketing aerosol models and their corresponding amount (in %) among the 40 half-orbits.


This time, the amount of couples of aerosol models between 13 and 30 is 2.9 % (against 0.5 % in Fig. 2) and the amount of couples including at least one model 31 (IOP model) is 4.5 % (against 5.5 %).

## 4.2 Statistics on marine reflectance at 412 nm for different geometry classes

We subdivide data pixels by geometry classes. These classes are defined by constraining one parameter at a time while the others are left free:

- sun zenithal angle (between 20° and 80°): classes 20°-40°, 40°-60°, and 60°-80°
- viewing zenithal angle (between 0° and 40°): classes 0°-10°, 10°-20°, 20°-30°, and 30°-40°
- delta azimuthal angle (between 0° and 180° with two peaks at about 45° and 135°): classes 0°-45°, 45°-90°, 90°-135°, 135°-180°
- diffusion angle (between 0° and 107°): classes 0°-20°, 20°-40°, ... 80°-100°

Considering Figure 18 it is impossible to investigate all couples. However, it is possible to separate the analysis into numerous cases of diagonal and non-diagonal couples. In each category a selection of relevant geometry cases are shown.

	SENTINEL-3 OPTICAL PRODUCTS AND ALGORITHM DEFINITION  ERROR PROPAGATION IN THE ATMOSPHERE CORRECTION	REF: S3-L2-SD-01-C01-ACR-TN VERSION: 1.2 DATE: 30 SEPTEMBER 2010 PAGE 27
--	---	---

#### 4.2.1 *Statistics for diagonal couples*

Figure 19 shows the standard deviation of  $\rho_w$  at 412 nm for six diagonal couples and including all geometries. For all models (except couple (21,21))  $\sigma_p$  is comparable to  $\sigma_p$  obtained for the couple (0,0) on Figure 14. For models (0,0), (31,31) and (2,2), which have the highest statistics, a second branch of  $\sigma_p$  is visible. It might consist of marginal artefacts induced by neighbouring sun-glint, cases of turbid waters, or other sources of uncertainty from the previous steps of the MEGS data processing.

Figure 20 and Figure 21 now detail the cases of couples (0,0) and (31,31) for some geometry classes, they show that  $\sigma_p$  is only slightly influenced by the geometry in the case of diagonal couples.

#### 4.2.2 *Statistics for non-diagonal couples*

Figure 22 shows  $\sigma_p$  for non-diagonal couples (0,4), (3,7), (4,8), (5,12), (9,31), and (18,15) and Figure 23 and Figure 24 detail the cases of couples (0,4) and (5,12) for some geometry classes. From Figure 24 we see that **the uncertainty is larger for non-diagonal couples than for diagonal couples and can vary greatly from one couple to another** (for example couples (0,4) and (9,31)). This is because error is propagated on two models instead of only one.

By varying geometry most couples, taken independently, do not exhibit a large variability with regard to geometry (not shown). In Figure 23 and Figure 24 we show that it cannot be concluded for all couples. Indeed the couple (0,4) and, on a larger extent, the couple (5,12), exhibit different modes and/or amplitudes. In the case of the couple (0,4) this cannot be related to turbid water cases (discriminated using BPAC\_ON = 1) within the whole statistics since this amount is smaller than 10 % (and usually around 1 %) in every panel of Fig. 23.

However, in the case of the couple (5,12), where the modes and amplitudes of the uncertainty have the largest variability, the amount of turbid water cases is abnormally high (about 40-60 %) with many possible sensitive cases. In Figure 24 this amount is (resp.) 39 and 62 % for the two sun zenithal angles classes and possibly induces the observed discrepancy. Therefore it is likely that, for the couple (5,12) (the 'worst' case), the differences are induced by additional uncertainties from turbid water corrections. Figure 25 compares statistics from the couple (5,12) for all geometries but separately for originally not turbid cases (BPAC\_ON = 0, therefore case 1 and sensitive cases) (left) and for originally turbid cases (BPAC\_ON = 1) (right). Also, the top case are from stable aerosols while the bottom cases are from all aerosols (stable + unstable). Although turbid cases induce higher uncertainties there is no clear separation between the two modes appearing in these figures. Using all aerosols instead of stable aerosols provides more statistics but do not significantly change this result as the amount of unstable cases is usually small compared to the stable cases.

**The influence of stability and turbidity will more explicitly appear in the next section as we will show a method for the computation of water-leaving reflectance variance for stable aerosols over clear waters. This method implies the construction of LUTs.**

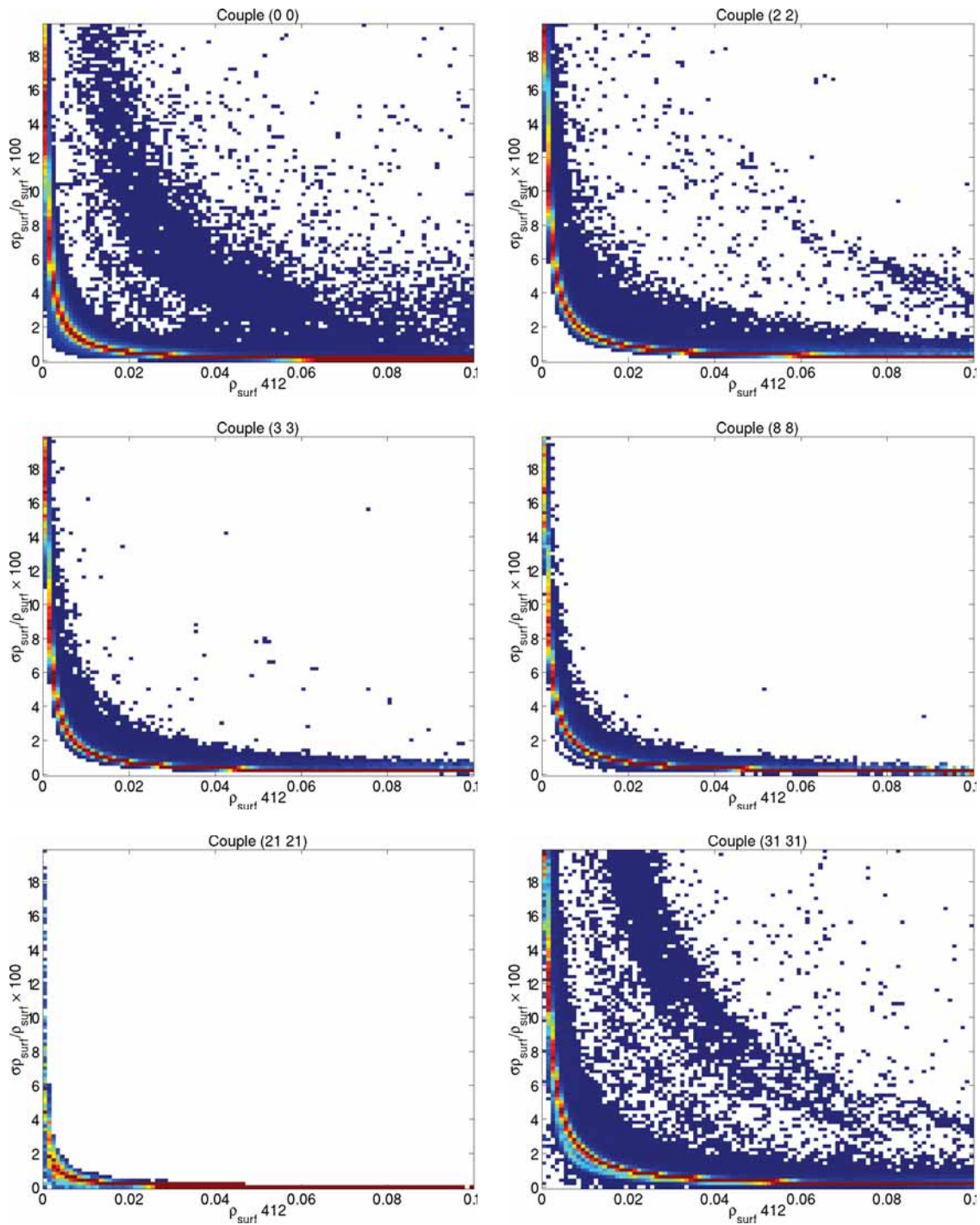
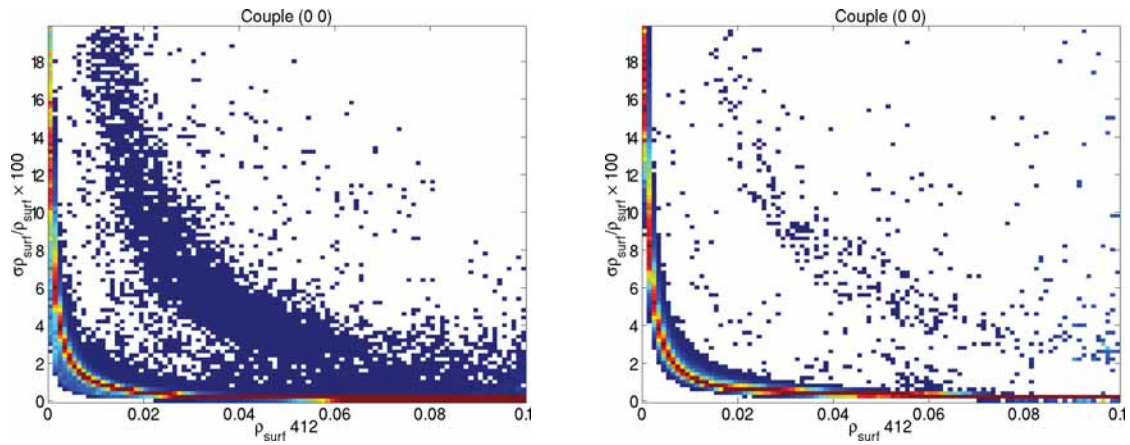
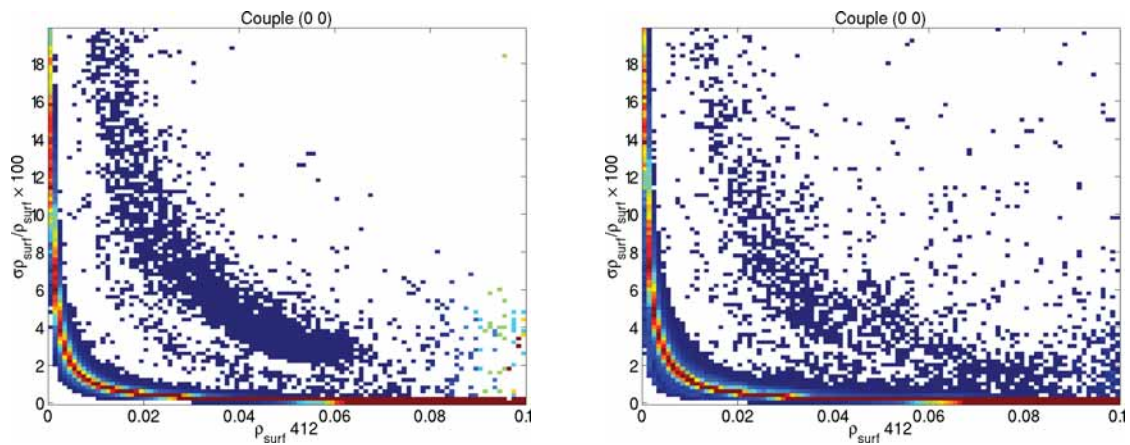


Figure 19: Stable aerosols, all geometries. Six different pairs of diagonal bracketing aerosol models: (0,0), (2,2), (3,3), (8,8), (21,21), and (31,31).

Sun zenithal angle: left, 20°-40°, right, 60°-80°



Viewing zenithal angle: left, 0°-10°, right, 30°-40°



Diffusion angle: left, 20°-40°, 80°-100°

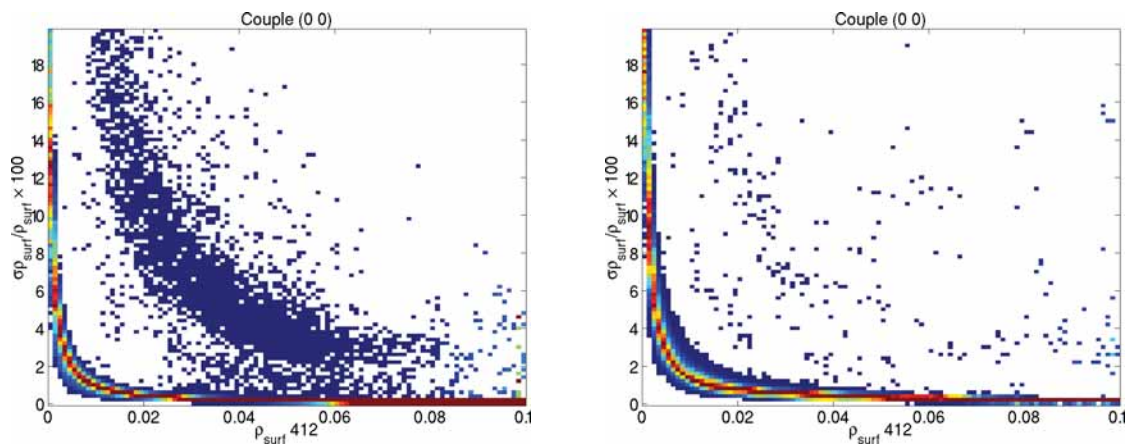
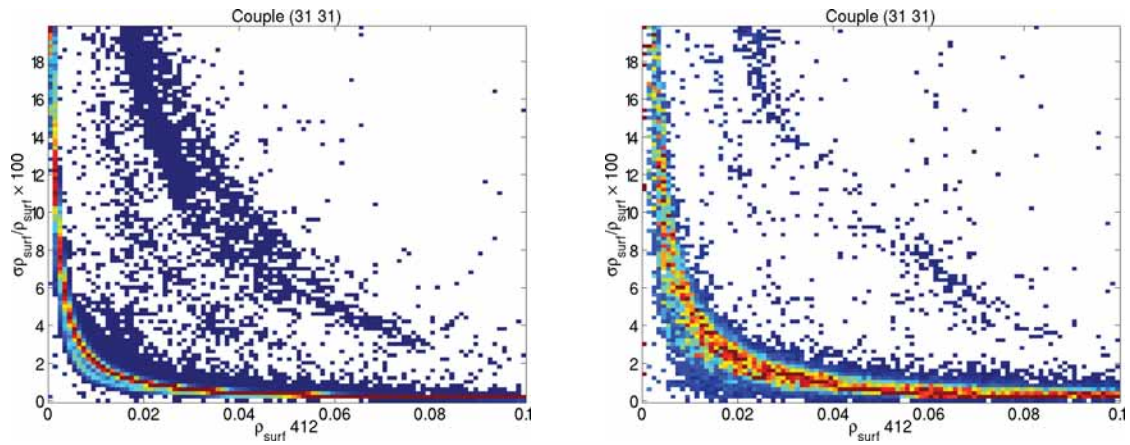
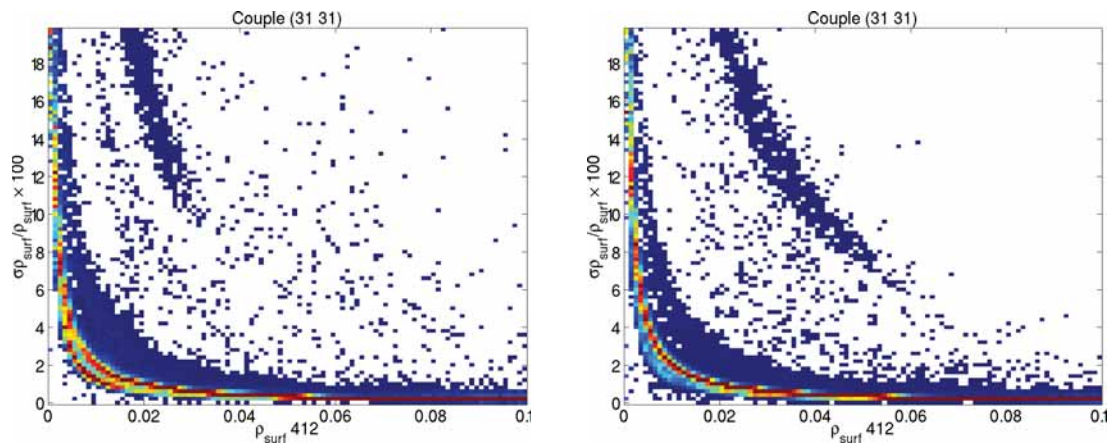


Figure 20: Couple (0, 0), different geometries.

Sun zenithal angle: left, 20°-40°, right, 60°-80°



Viewing zenithal angle: left, 10°-20°, right, 30°-40°



Diffusion angle: left, 0°-20°, 80°-100°

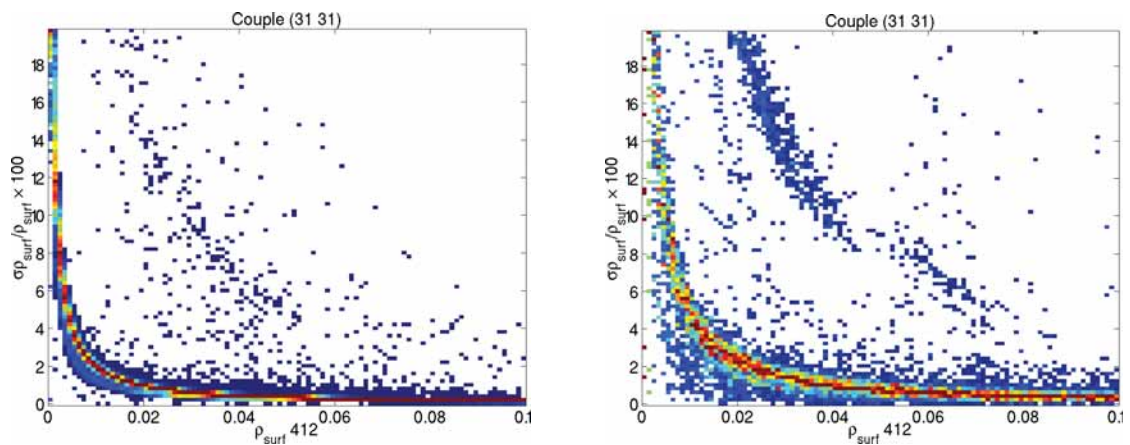


Figure 21: Couple (31, 31), different geometries.

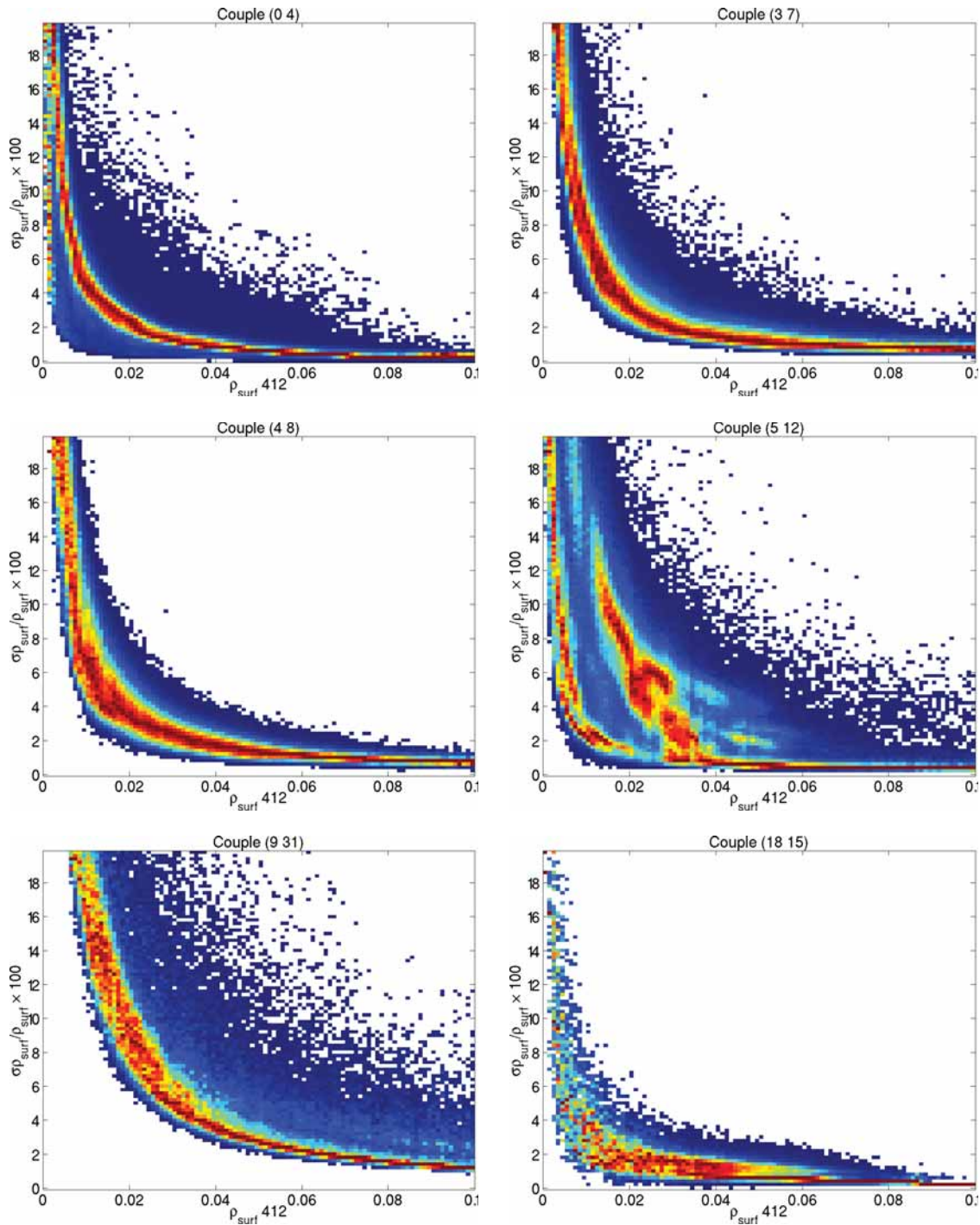
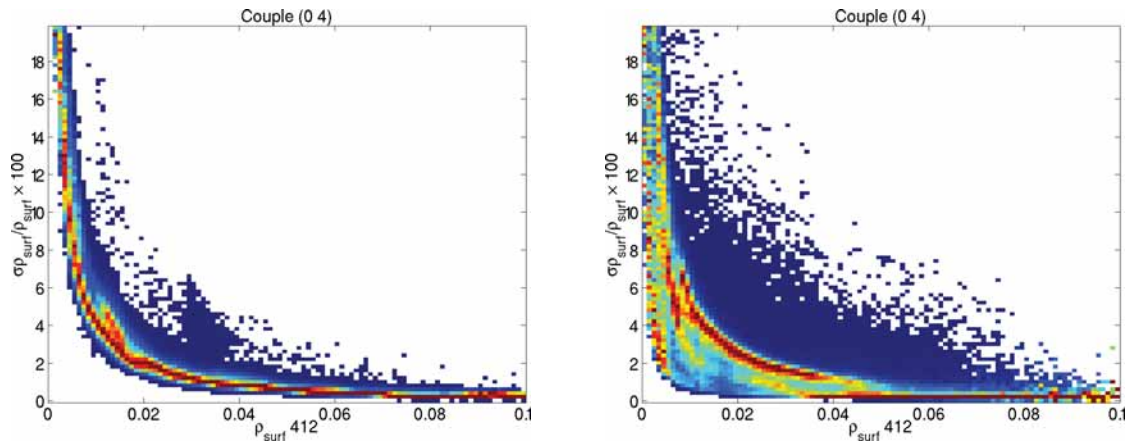
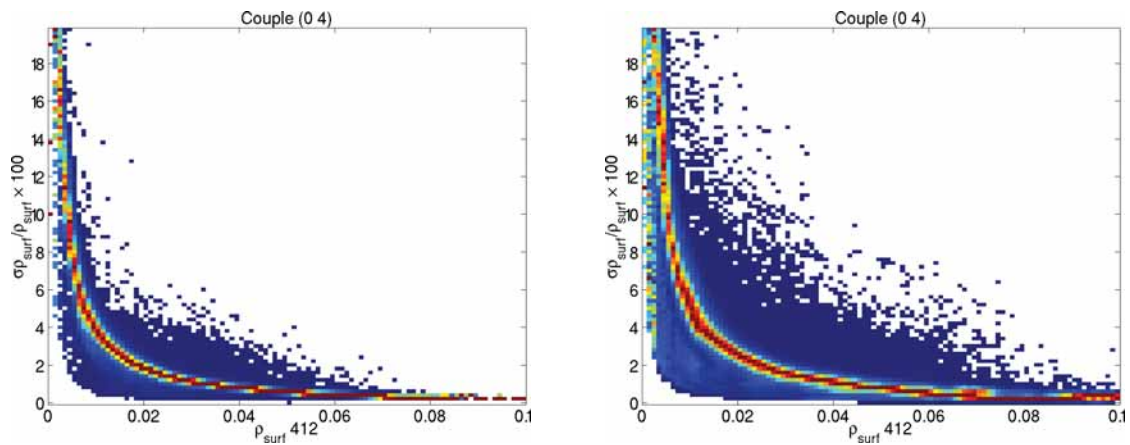


Figure 22: Stable aerosols, all geometries. Six different pairs of non-diagonal bracketing aerosol models: (0,4), (3,7), (4,8), (8,8), (9,31), and (18,15).

Sun zenithal angle: left, 20°-40°, right, 60°-80°



Viewing zenithal angle: left, 0°-10°, right, 30°-40°



Diffusion angle: left, 20°-40°, 80°-100°

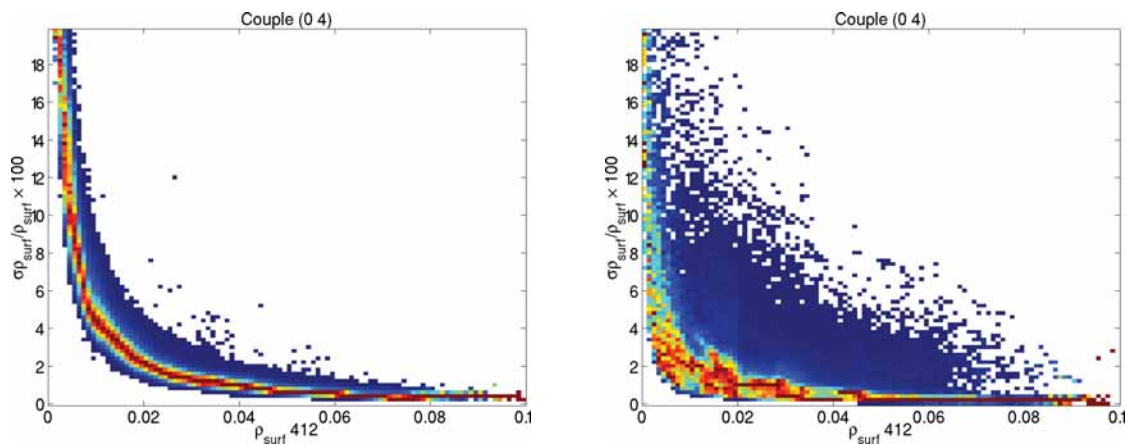
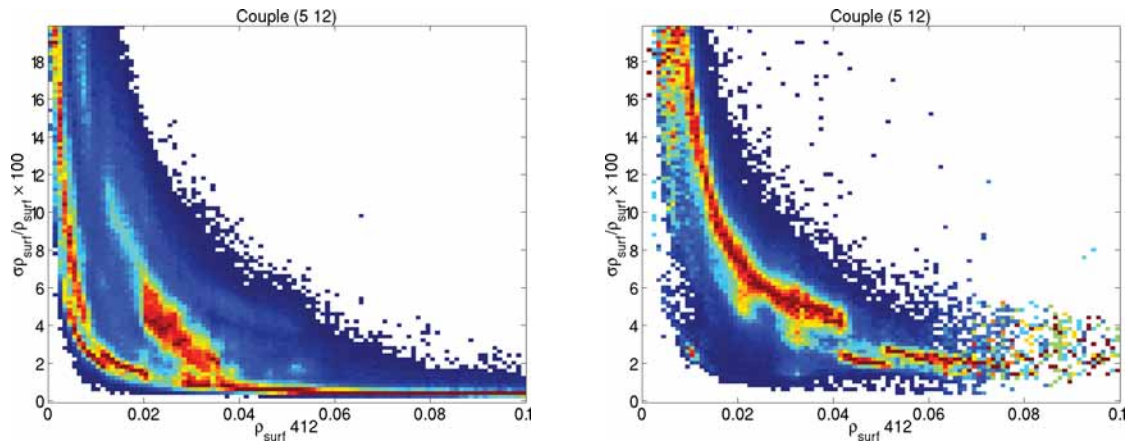
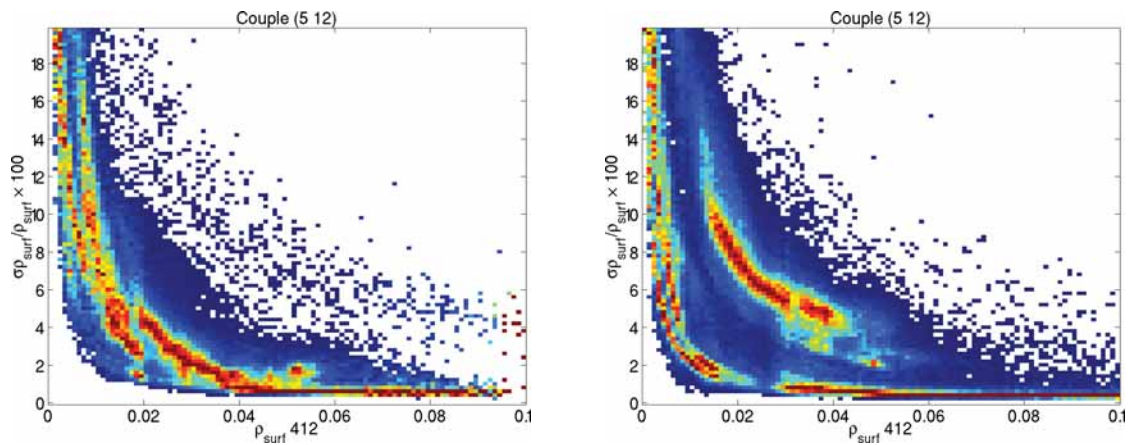


Figure 23: Couple (0, 4), different geometries.

Sun zenithal angle: left, 20°-40°, right, 40°-60°



Viewing zenithal angle: left, 0°-10°, right, 30°-40°



Diffusion angle: left, 0°-20°, 60°-80°

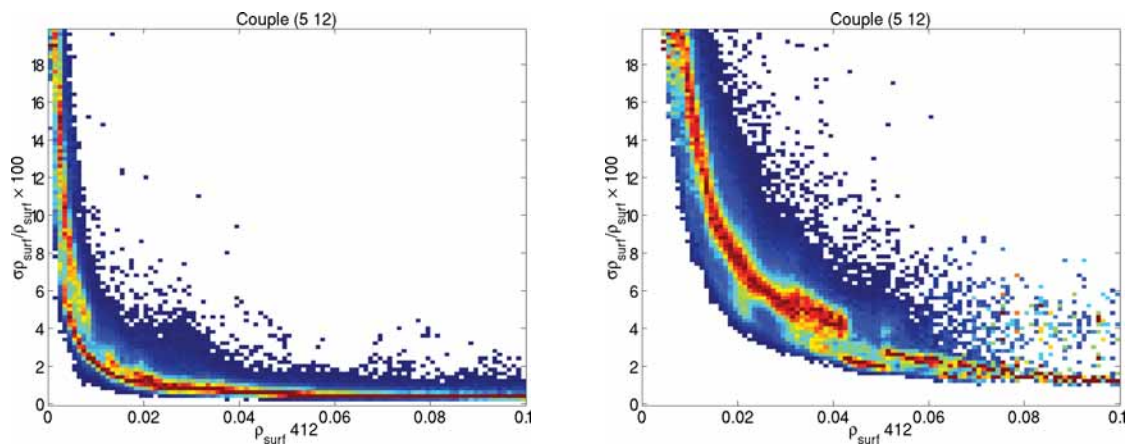
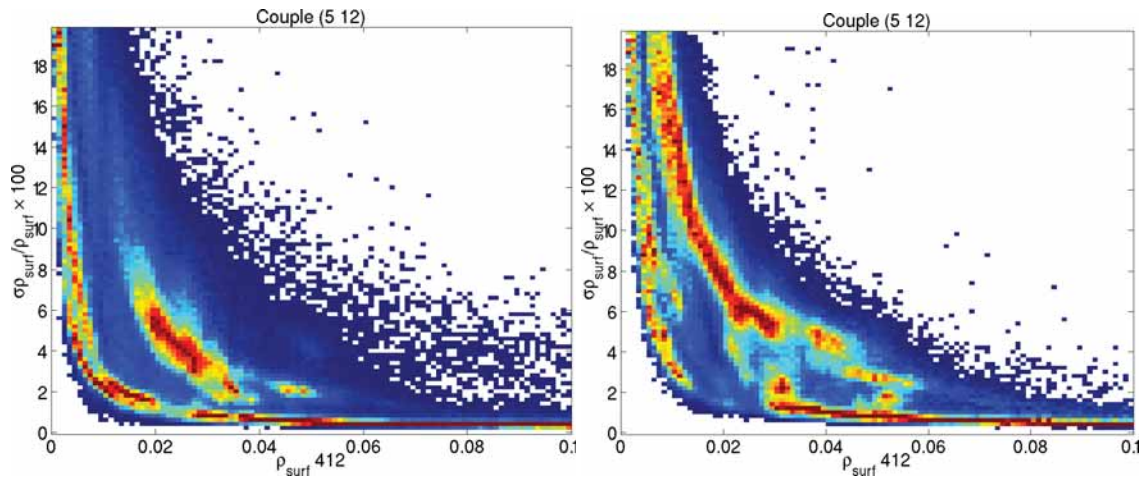


Figure 24: Couple (5, 12), different geometries.

Stable aerosols:



All aerosols (stable + unstable):

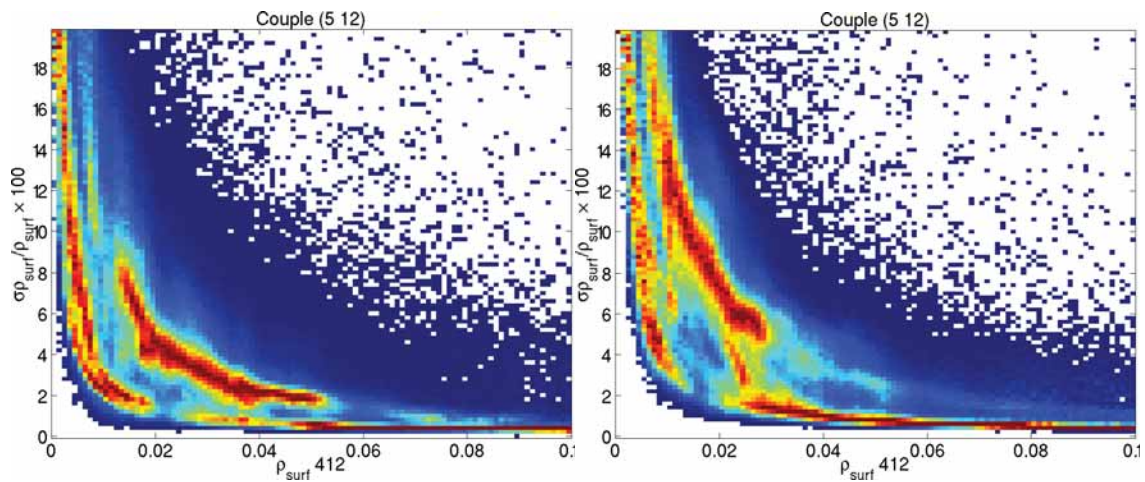



Figure 25: Couple (5, 12), not originally turbid (left) and originally turbid (right). Stable models (top) and all models (bottom).

	SENTINEL-3 OPTICAL PRODUCTS AND ALGORITHM DEFINITION  ERROR PROPAGATION IN THE ATMOSPHERE CORRECTION	REF: S3-L2-SD-01-C01-ACR-TN VERSION: 1.2 DATE: 30 SEPTEMBER 2010 PAGE 35
--	---	---

## 5 LOOK-UP TABLES FOR UNCERTAINTY ESTIMATION

As shown in the previous sections by using a loop into the processing, the uncertainty of the output reflectances can be computed and stored with other variables. However the processing of each pixel is time consuming and uses a lot of resources.

Therefore, we rather investigate a method of estimating uncertainties based on the construction of Look-up tables (LUTs) which will be called during data retrieval. These LUTs will be computed, once and for all, for each aerosol couple and geometry.

There are two possible approaches but one is preferred. They both consist in estimating the uncertainty  $\sigma_{pw}$  over the water-leaving reflectances  $\rho_w$ .

In both cases the LUTs will strongly depend on the definition of the input noise which remains to be clearly defined. In this section we still use the 'B02' additive Gaussian noise.

### 5.1 Method using the $(\sigma_{pw}, \rho_w)$ histograms

In the previous sections we have shown that the uncertainty  $\sigma_{pw}$  generally follows a smooth relationship as a function of  $\rho_w$ . Apart from sensitive cases these relationships are well defined by the median curve of the histograms: for each interval of  $\rho_w$  the median can be computed. As opposed to the mean it has the advantage of reducing the influence of artefacts arising from other sources of uncertainty in MEGS (such as glint or optically thin clouds) in the statistics. These sources of uncertainty are traced and flagged during data retrieval and therefore can be ignored.

For the couple (4, 8) and for one specific geometry Figure 26 shows the  $(\sigma_{pw}, \rho_w)$  histogram and its corresponding median curve. The median can be fitted and its coefficients stored in LUTs.

Specific attention should be drawn for turbid water cases as well as for unstable cases (either clear or turbid waters). In the first case specific LUTs could be built directly from turbid only cases. In the latter case LUTs should be built without taking into account possible departures from the original aerosol bracketing couple.

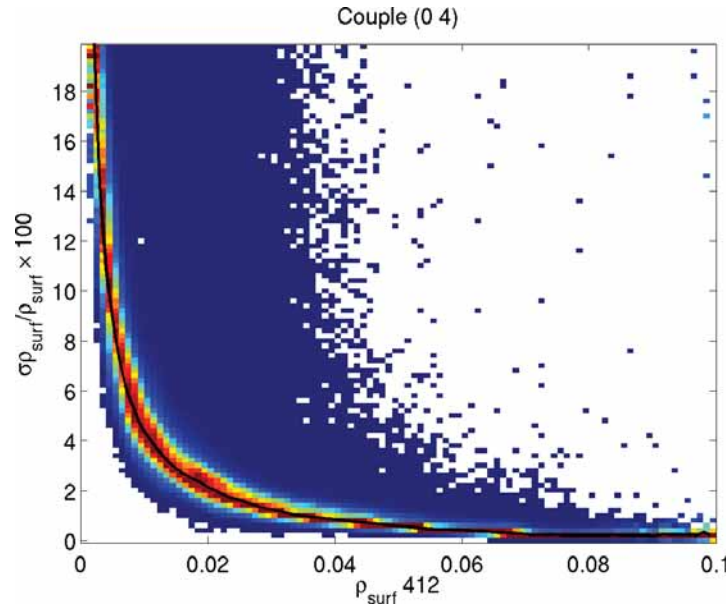


Figure 26: Standard deviation of  $\rho_w$  (normalized by  $\rho_w$ ) for couple (4,8) and its median curve.

This method is straightforward but only considers a direct relationship between  $\rho_w$  and its uncertainty. As a consequence, it is not possible to separate the influence of the error which is propagated from the NIR and the contribution of the error directly arising from channel radiance noise at the investigated wavelength (other than NIR). Therefore, the second method (below) is preferred.

## 5.2 Method using other variables


The starting point of the second method is the relationship between the TOA reflectance  $\rho_{TOA}$ , the total transmittance  $t$ , the atmospheric path reflectance and the water-leaving reflectance  $\rho_w$ :

$$\rho_w = (\rho_{TOA} - \rho_{pathstar}) / t$$

At the moment we are only interested in the uncertainty arising from the atmospheric correction module, therefore we assume that no uncertainty arises from  $\rho_{TOA}$  yet. However, for a total error budget this uncertainty must be taken into account. We might then use  $\text{Var}(\rho_{TOA} - \rho_{pathstar}) = \text{Var}(\rho_{TOA}) + \text{Var}(\rho_{pathstar})$ .

Without TOA error it can be shown by means of a Taylor expansion that an estimation of  $\text{Var}(\rho_w)$  is

$$\begin{aligned} \text{Var}(\rho_w) \approx & (1/t^2) * \text{Var}(\rho_{pathstar}) + 2 * ((\rho_{TOA} - \rho_{pathstar})/t^3) * \text{Cov}(\rho_{pathstar}, t) \\ & + ((\rho_{TOA} - \rho_{pathstar})^2 / t^4) * \text{Var}(t) \end{aligned}$$

	SENTINEL-3 OPTICAL PRODUCTS AND ALGORITHM DEFINITION  ERROR PROPAGATION IN THE ATMOSPHERE CORRECTION	REF: S3-L2-SD-01-C01-ACR-TN VERSION: 1.2 DATE: 30 SEPTEMBER 2010 PAGE 37
---	---	---

We have tested this formula by comparison to the noise outputs of  $\rho_w$ , a perfect correlation was found (not shown).

The variance (or standard deviation) and covariance terms can be tabulated as a function of the aerosol optical depth  $\tau_{aer}$ . The coefficients of the interpolating polynomials will be stored as LUTs.

The processing of a huge amount of orbits by MEGS (including the noise loop) will never provide enough statistics for all aerosol couples and geometries. To overcome this difficulty we propose a method which requires no specific input.

### 5.2.1 *Implementation of the method*

In the equation of  $\text{Var}(\rho_w)$  we need to interpolate  $\text{Var}(\rho_{\text{pathstar}})$ ,  $\text{Var}(t)$ , and  $\text{Cov}(\rho_{\text{pathstar}}, t)$  as a function of  $\tau_{aer}$  for each specific couple of bracketing models and each specific geometry. These quantities are independent of the observed situation ( $\rho_{\text{TOA}}$  and  $\rho_w$ ) and are only dependent on the geometry and the couple which is determined in the NIR.

Therefore,  $\text{Var}(\rho_{\text{pathstar}})$ ,  $\text{Var}(t)$  (or Std), and  $\text{Cov}(\rho_{\text{pathstar}}, t)$  can directly be determined by scanning the reflectances in the NIR channels 775 and 865 nm.

To do so, we follow the atmospheric correction algorithm implemented in MEGS. As explained previously, the latter consists in the determination of the couple of aerosols from the simulation of the ratio  $\rho_{\text{pathstar}} / \rho_R$  at 775 nm (where  $\rho_R$  stands for the Rayleigh reflectance) for all aerosol models when it is given at 865 nm. The two closest 775 nm simulated ratio to the one actually measured selects the two bracketing aerosol models 'aer 1' and 'aer 2'.


A loop is then performed on all possible ratios  $\rho_{\text{pathstar}} / \rho_R$  values at 865 nm, if one specific couple and geometry is selected we can compute the ratios  $\rho_{\text{pathstar}} / \rho_R$  at 775 nm for the two bracketing aerosol models. These two ratios at 775 nm then give the range in  $\rho_{\text{pathstar}} / \rho_R$  at 775 nm within which MEGS would find the two aerosols as best candidates for the retrieval.

In the range of  $\rho_{\text{pathstar}} / \rho_R$  at 775 nm the linearity inferred by the use of the aerosol mixing ratio implies the linearity of  $\tau_{aer}$ ,  $\rho_{\text{pathstar}} / \rho_R$  and  $\log(t)$  at all wavelengths. At one specific value of  $\rho_{\text{pathstar}} / \rho_R$  at 775 nm corresponds one mixing ratio and one value of these parameters which can all be computed using a linear fit of the values for the two bracketing solutions of  $\rho_{\text{pathstar}} / \rho_R$  at 775 nm for aer 1 and aer 2.

Therefore, for one specific value of  $\rho_{\text{pathstar}} / \rho_R$  at 865 nm a Gaussian noise simulation on  $\rho_{\text{pathstar}} / \rho_R$  at 775 nm can easily be conducted and the relationships between  $\text{Var}(\rho_{\text{pathstar}})$ ,  $\text{Var}(t)$  (or Std), and  $\text{Cov}(\rho_{\text{pathstar}}, t)$  as a function of  $\tau_{aer}$  can easily be obtained.

However, this only concerns a noise simulation on the 775 nm channel and not the independent but combined noise of both channels at 775 and 865 nm.

By looping on  $\rho_{\text{pathstar}} / \rho_R$  at 865 nm it is possible to make the loop step small enough to list a large amount of  $\rho_{\text{pathstar}} / \rho_R$  at 865 nm along with the bracketing parameters at all wavelengths. In an

	<p>SENTINEL-3 OPTICAL PRODUCTS AND ALGORITHM DEFINITION</p> <p>ERROR PROPAGATION IN THE ATMOSPHERE CORRECTION</p>	<p>REF: S3-L2-SD-01-C01-ACR-TN VERSION: 1.2 DATE: 30 SEPTEMBER 2010 PAGE 38</p>
---	---	---

independent but combined noise simulation on the 775 and 865 nm channels we are able to (first) noise the channel at 865 nm, (second) find the corresponding bracketing parameters when associating that noised value to the list of values of  $\rho_{\text{pathstar}} / \rho_R$  at 865 nm, and (three) compute rapidly the statistics for the determination of the LUTs by using the linearity at 775 nm.

In such way, all we need from MEGS is to build a list of values of the parameters incremented by values of  $\rho_{\text{pathstar}} / \rho_R$  at 865 nm which employs the aerosol LUTs implemented in MEGS. This is done by geometry and aerosol couples. To speed up, we determine the possible geometries and aerosol couples to avoid building useless LUTs. This is done by scanning all values of  $\rho_{\text{pathstar}} / \rho_R$  at 775 nm given by the aerosol models and for a large range of  $\rho_{\text{pathstar}} / \rho_R$  at 865 nm.

**The LUTs are defined so that they best compare to the stable aerosol observations of case 1 waters.** It makes no sense to try to define LUTs for unstable cases as departing aerosols may take different paths (toward different couples) and the concomitant increase of the uncertainty may be a function of the path. There exists a large amount of paths and there is no way to infer the proportions of every path for each observation. Rather, we will employ the LUTs determined for stable cases and will further examine possible biases inferred by considering all the cases. The same observation can be made for turbid waters although turbidity is explicitly declared (flagged) in the retrieval and can be considered with more caution.

For all aerosol couples between 0 and 12 (not absorbing) Figure 27 shows (left, all geometries combined) the percent amount of the steps of  $\rho_{\text{pathstar}} / \rho_R$  at 865 nm for which each couple was found. As suggested in the previous sections we find the usual predominant couples such as (0,4), (4,8), (5,12)... However, there is a large amount of the couple (10,9), which is unusual, most probably because the stepping values of  $\rho_{\text{pathstar}} / \rho_R$  at 865 nm are 'pushed' up to high values so that all possible cases (although rare) are taken into account with equal probability. As expected, other unusual couples appear in much smaller quantities.

The right figure shows the amount of geometry configurations for each couple, it shows that only about half of the LUTs should be computed (47.9 % exactly).

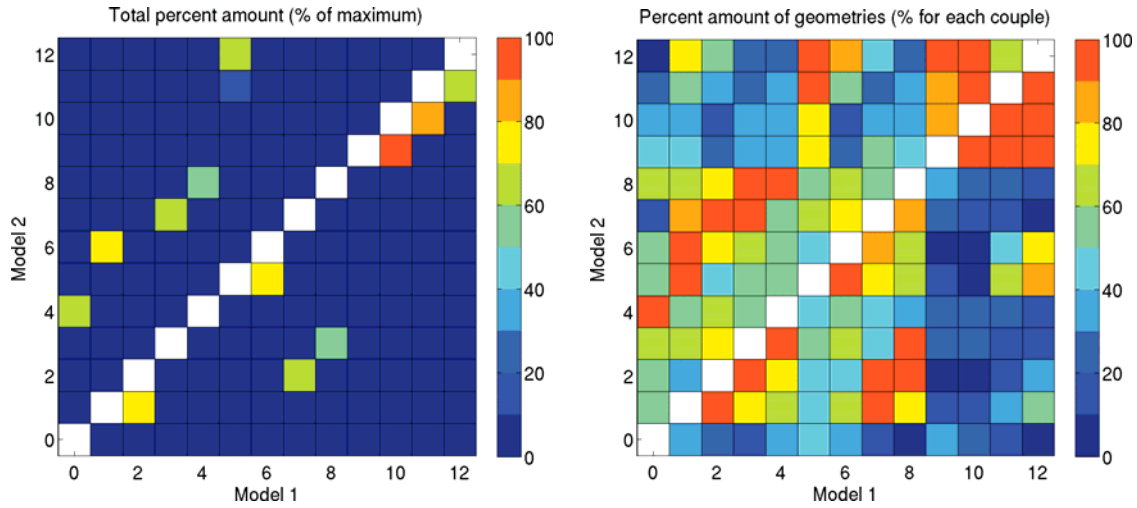


Figure 27: Left: percent amount of the steps of ppathstar / pR at 865 nm for which a couple was find. Right: amount of geometry configurations for each couple.

For the couple (4,8) and for a specific geometry, Figure 28 shows an example of the relationships obtained between  $\text{Std}(\rho_{\text{pathstar}})$ ,  $\text{Std}(t)$ , and  $\text{Cov}(\rho_{\text{pathstar}}, t)$  and  $\tau_{\text{aer}}$  at 412 nm as well as the fit of these relationships (order 5 polynomial used).

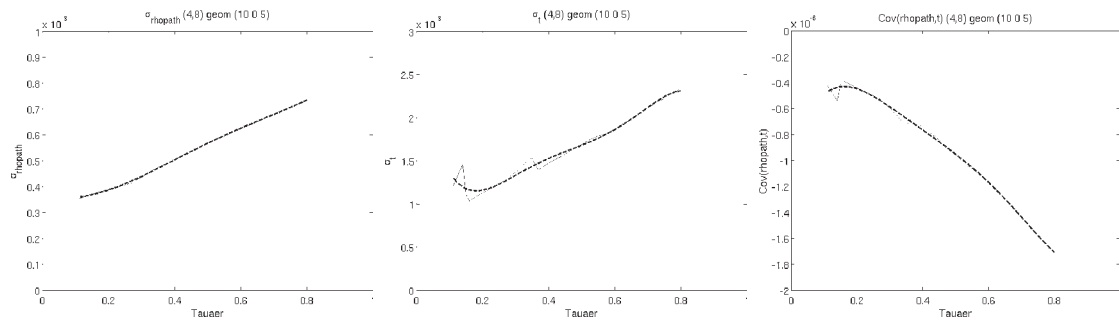



Figure 28: Relationships between  $\text{Std}(\rho_{\text{pathstar}})$ ,  $\text{Std}(t)$ , and  $\text{Cov}(\rho_{\text{pathstar}}, t)$  and  $\tau_{\text{aer}}$  at 412 nm obtained for the couple (4,8) at one geometry grid point ('10 0 5').

As LUTs are determined on specific geometry grid points (the same as the aerosol LUTs) the calculation of the uncertainties over  $\rho_w$  is made by interpolating the coefficients of the LUTs at the eight surrounding geometry grid points for each observation. In MEGS, when one pixel is being processed, it is possible that one couple of aerosols is called for which not all eight nodes of the 'geometry cube' have computed LUTs. This leads to errors in interpolating LUTs.

	SENTINEL-3 OPTICAL PRODUCTS AND ALGORITHM DEFINITION  ERROR PROPAGATION IN THE ATMOSPHERE CORRECTION	REF: S3-L2-SD-01-C01-ACR-TN VERSION: 1.2 DATE: 30 SEPTEMBER 2010 PAGE 40
--	---	---

To overcome this situation, LUTs have been processed for all geometry nodes for which these couples are called as well as for the neighbouring nodes. As a consequence, a total of 62 % of the geometry nodes need the computation of the LUTs (only for aerosols lower than or equal to 12).

Values of  $\text{Var}(\rho_{\text{pathstar}})$ ,  $\text{Var}(t)$ , and  $\text{Cov}(\rho_{\text{pathstar}}, t)$  are first extracted and  $\text{Var}(\rho_w)$  is finally computed using the uncertainty equation. The calculated values can be compared to the ones obtained from the Monte-Carlo simulations.

### 5.2.2 Comparisons for stable couples over case 1 waters

For some of the most occurrent couples, Figure 29 and Figure 30 show the distributions of the relative difference  $(\text{calc-simu})/\text{simu} \times 100 \%$  (left) and of the mean (over all  $\rho_w$  values) relative difference (right) between the uncertainties at 412 nm obtained by the calculation using the LUTs and by Monte-Carlo simulations.

**The relative difference is always small and not significantly biased. The variability echoes the variability of the simulated error.**

Figure 31 shows one result (couples (4,8)) at wavelength 560 nm.

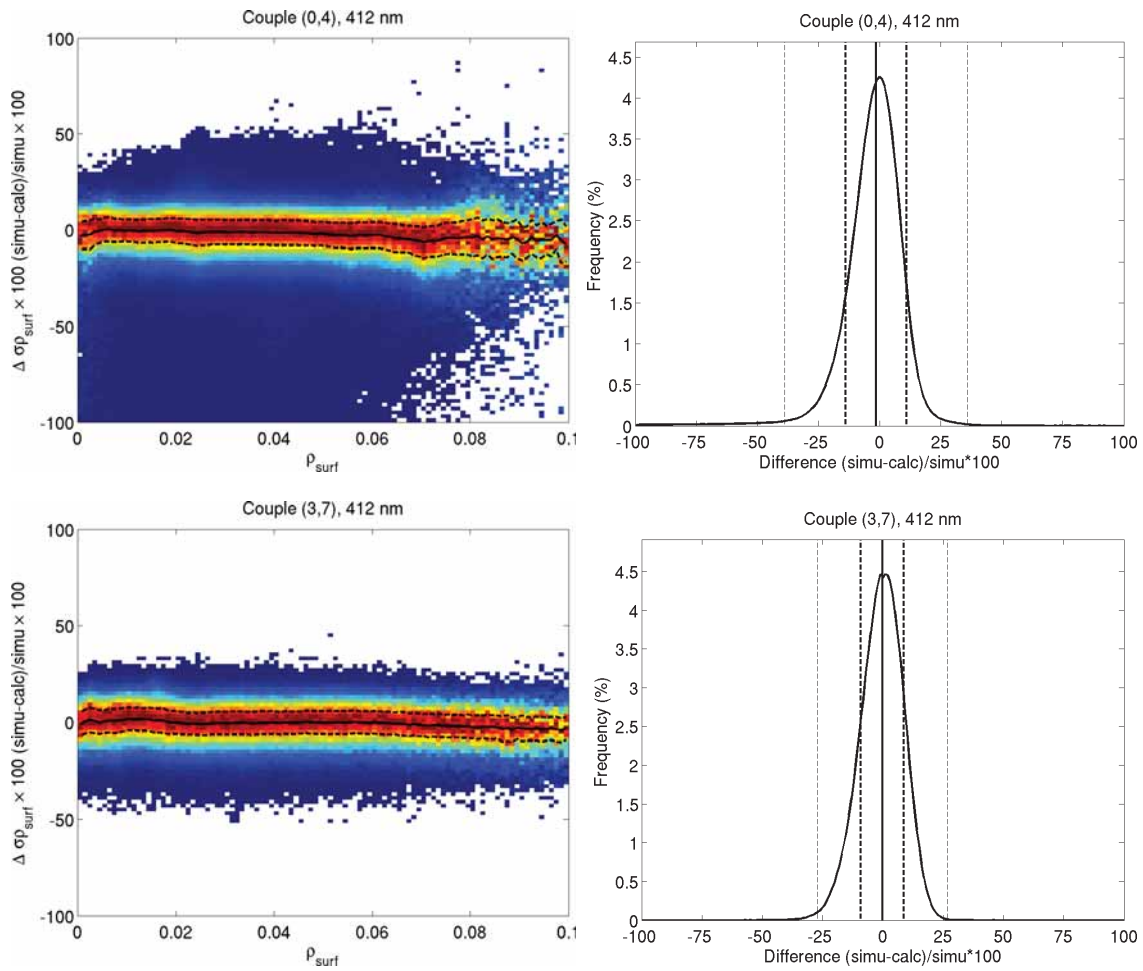


Figure 29: Relative difference between the simulated and the calculated uncertainties  $\text{std}(\rho_w)$  as a function of  $\rho_w$  for **stable** observations of **case 1** waters. Couples (0,4) and (3,7), 412 nm.

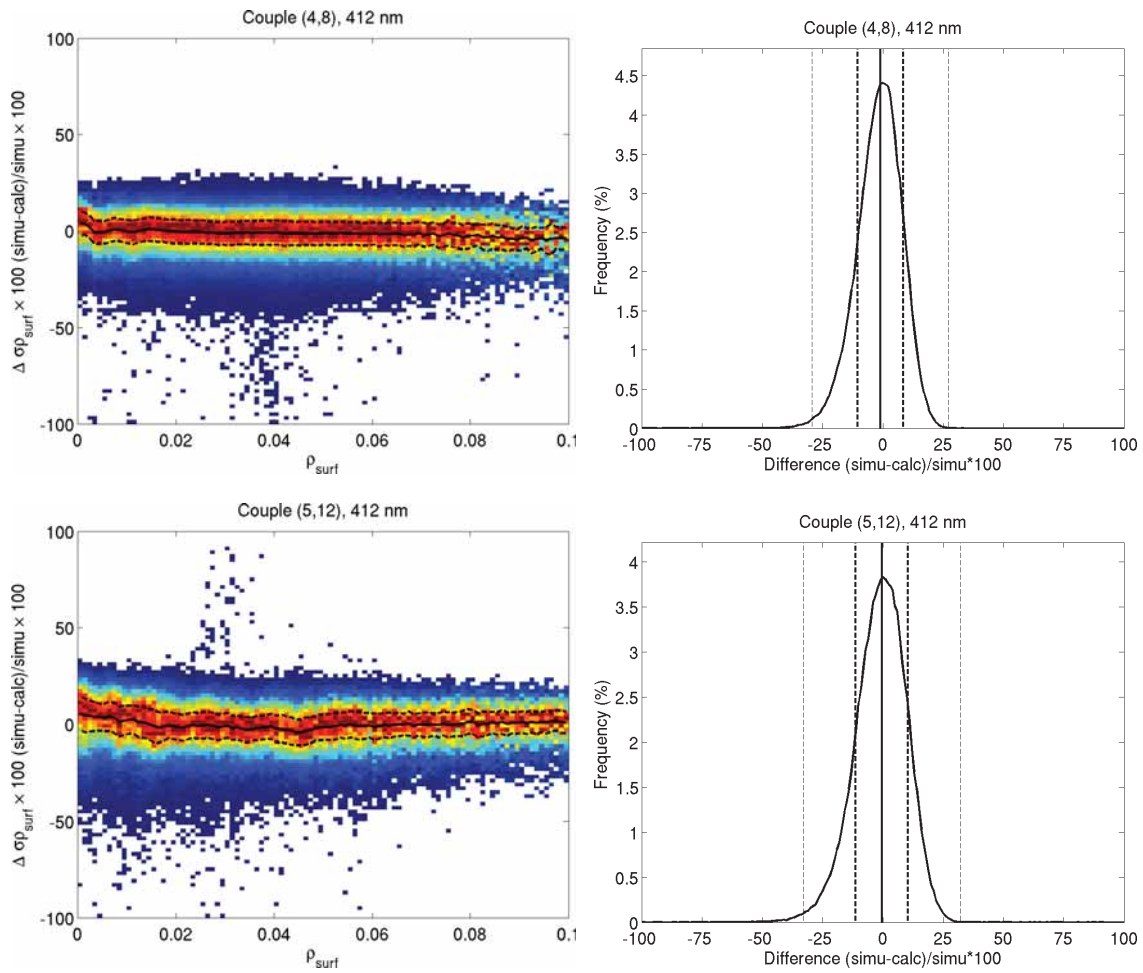


Figure 30: Relative difference between the simulated and the calculated uncertainties  $\text{std}(\rho_w)$  as a function of  $\rho_w$  for **stable** observations of **case 1** waters. Couples (4,8) and (5,12), 412 nm.

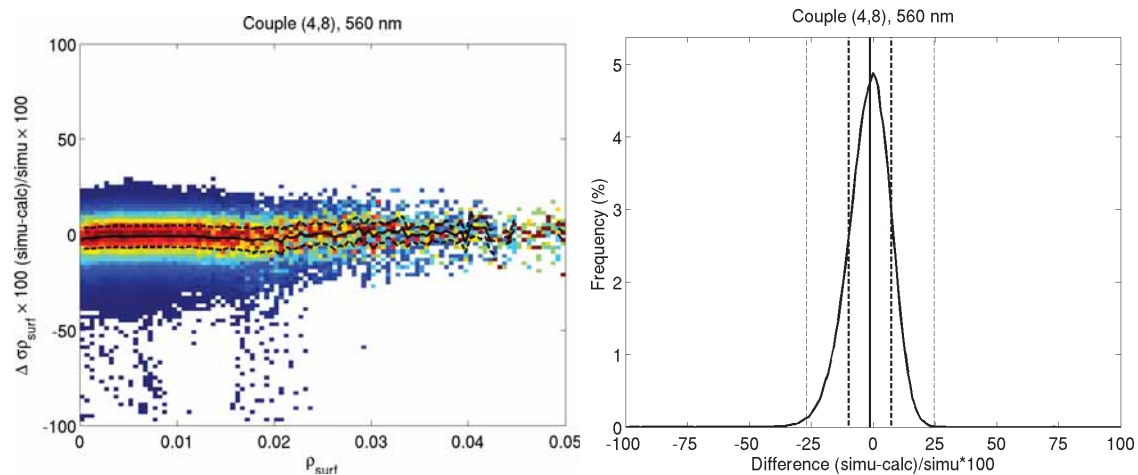


Figure 31: Relative difference between the simulated and the calculated uncertainties  $\text{std}(\rho_w)$  as a function of  $\rho_w$  for **stable** observations of **case 1** waters. Couples (4,8), 560 nm.

### 5.2.3 Comparisons for all couples (stable + unstable) over case 1 waters

Without simulating noise there is no possible distinction of stable and unstable cases when pixels are being processed. Therefore it is important to evaluate the use of the LUTs (which predicts noise for stable cases) for all cases of stability.

Figure 32 and Figure 33 show the same comparisons but when considering stable and unstable couples. It now provides a quantitative view of the effect of the departure of the aerosol models when the noise is applied. In fact, it compares the simulated noise (stable and unstable cases) to the computed noise which does not consider departures of the models.

We therefore see spreads in distributions of the relative difference between these two quantities. These spreads vary from one couple to another as the proportions and the paths of the departures are different. On average, the computed noise is larger than the simulated one with about 25 % relative difference. Thus, on a practical basis, computed noise is a higher boundary of the 'real' noise when no distinction is possible between stable and unstable cases. It overestimates noise of about 25 %.

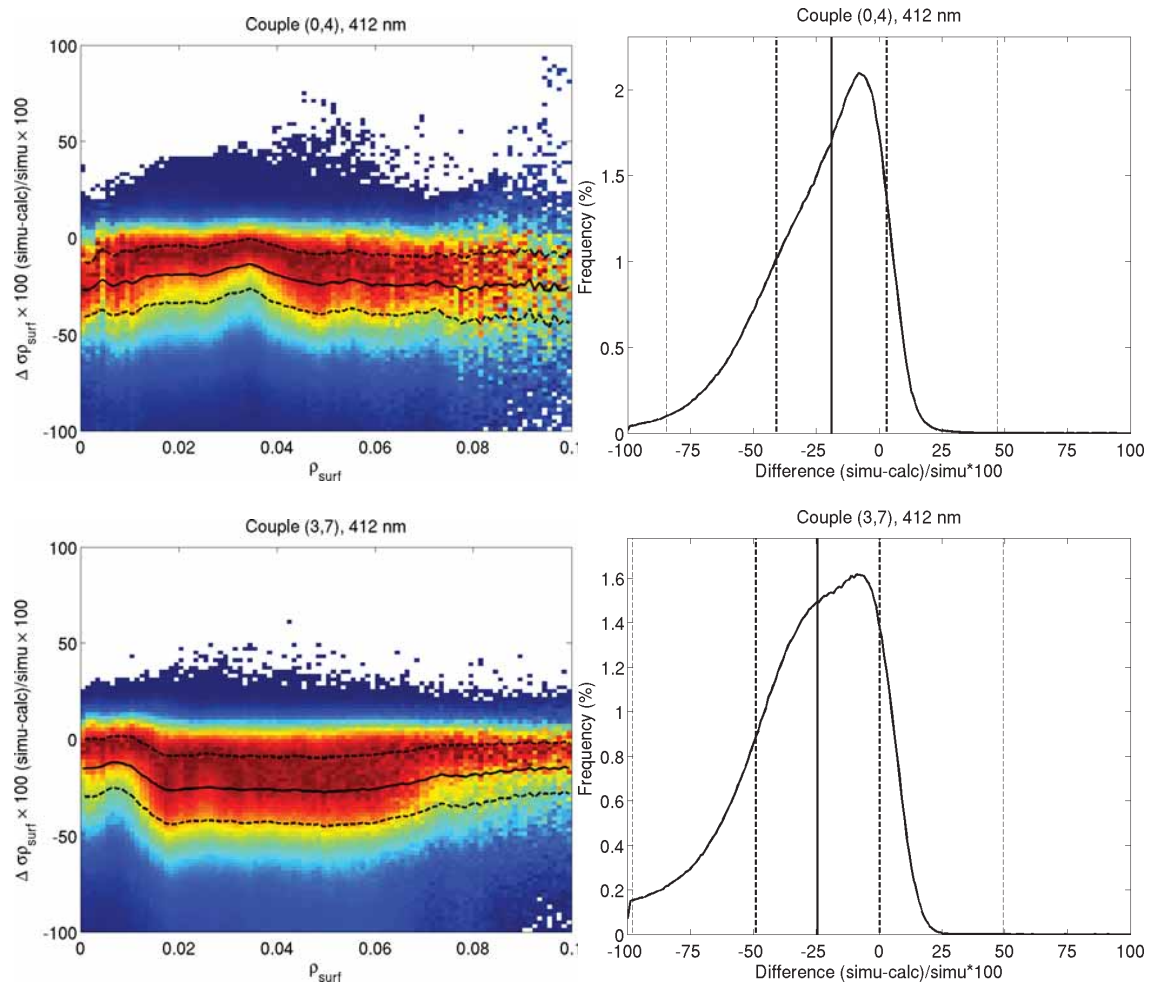


Figure 32: Relative difference between the simulated and the calculated uncertainties  $\text{std}(\rho_w)$  as a function of  $\rho_w$  for all (stable + unstable) observations of **case 1** waters. Couples (0,4) and (3,7), 412 nm.

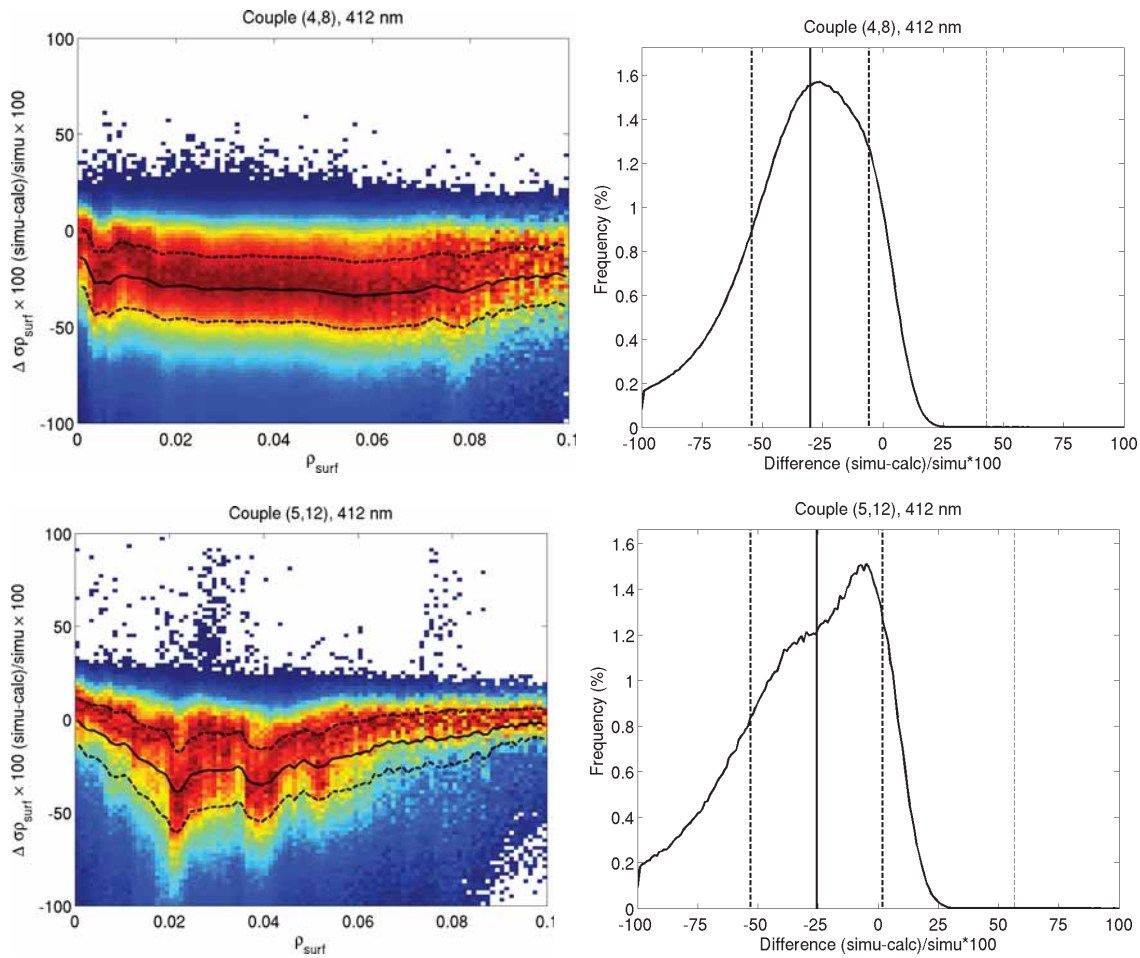


Figure 33: Relative difference between the simulated and the calculated uncertainties  $\text{std}(p_w)$  as a function of  $p_w$  for **all** (stable + unstable) observations of **case 1** waters. Couples (4,8) and (5,12), 412 nm.

#### 5.2.4 Comparisons for stable couples over turbid waters

As for the stability the effect of processing turbidity can be seen on the comparison between simulated and computed noise when the observed scenes are detected as turbid and processed as such in MEGS. This time, turbidity induces more noise through the MEGS processing chain. LUTs underestimate noise of about 25 % when the scene is turbid.

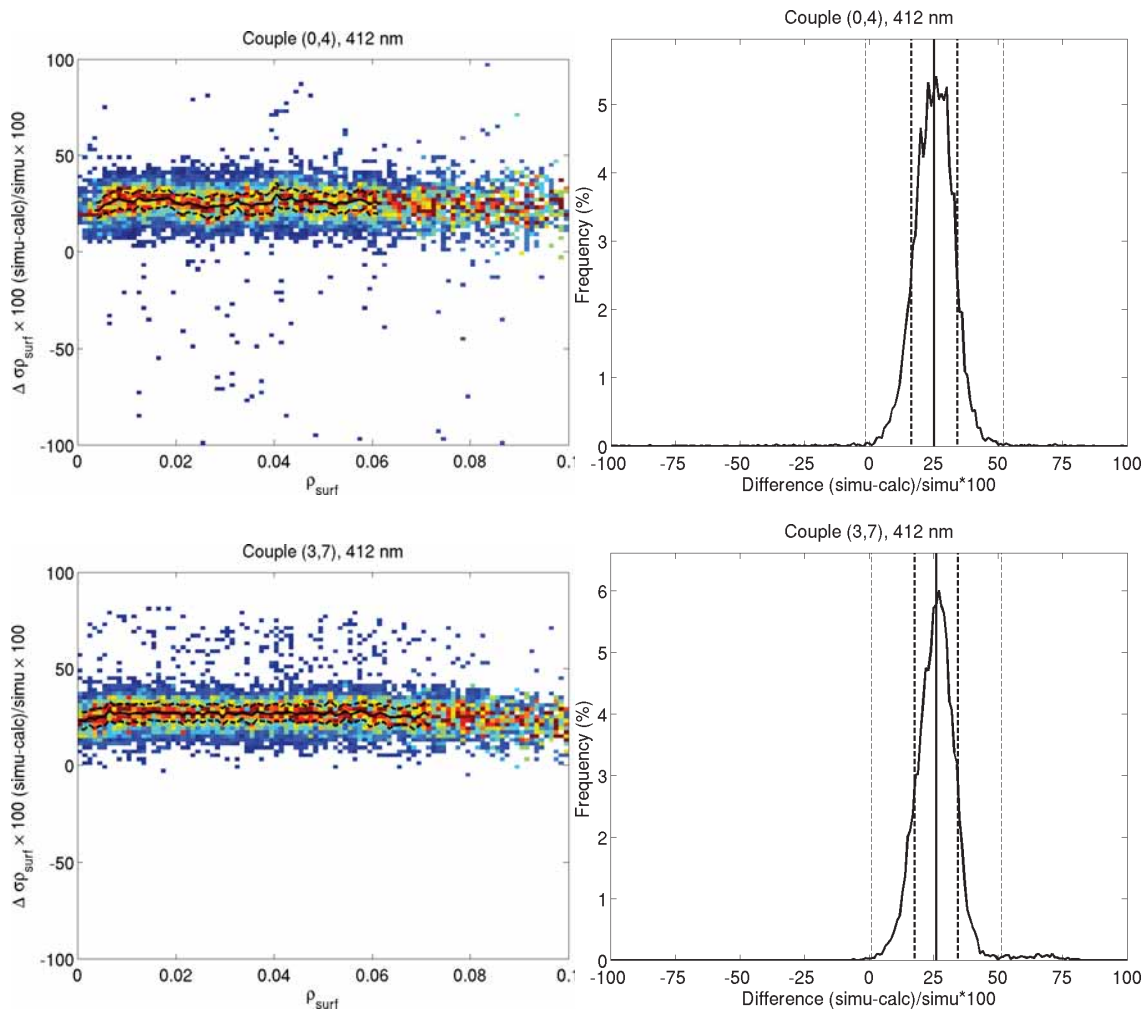


Figure 34: Relative difference between the simulated and the calculated uncertainties  $\text{std}(\rho_w)$  as a function of  $\rho_w$  for **stable** observations of **turbid** waters. Couples (0,4) and (3,7), 412 nm.

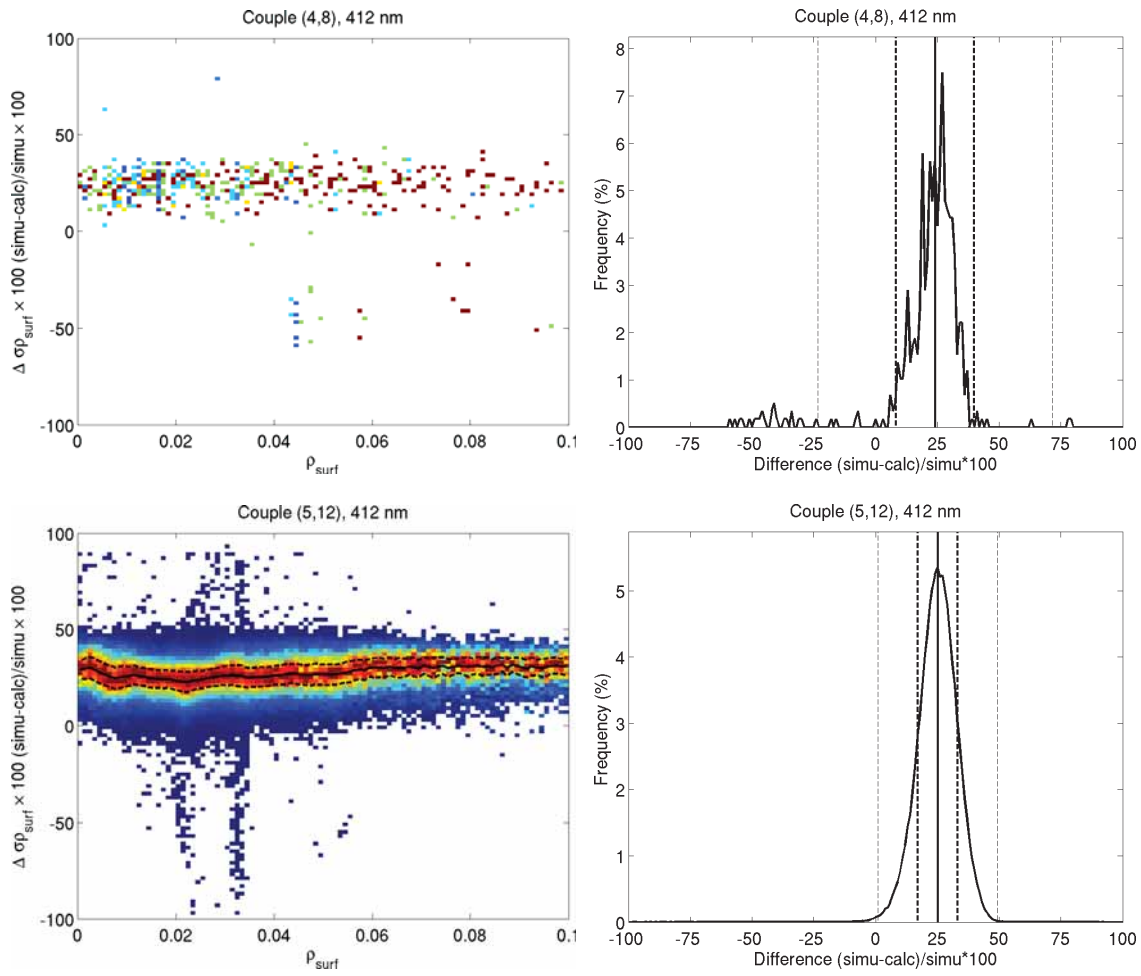



Figure 35: Relative difference between the simulated and the calculated uncertainties  $\text{std}(\rho_w)$  as a function of  $\rho_w$  for **stable** observations of **turbid** waters. Couples (4,8) and (5,12), 412 nm.

	<p>SENTINEL-3 OPTICAL PRODUCTS AND ALGORITHM DEFINITION</p> <p>ERROR PROPAGATION IN THE ATMOSPHERE CORRECTION</p>	<p>REF: S3-L2-SD-01-C01-ACR-TN VERSION: 1.2 DATE: 30 SEPTEMBER 2010 PAGE 48</p>
--	---	---

## 6 SYNTHESIS

We have performed additive Gaussian noise on the two NIR wavelengths used for the determination of aerosol properties in the atmospheric correction algorithm of MEGS. Statistics of departures from the original retrieval (selection of aerosol models, marine reflectances...) have firstly been computed over one half-orbit of MERIS observations. In some cases the selected aerosol models can depart from the original couple ('unstable' aerosol models) and adding noise may avoid/induce turbid water corrections although the original solution is detected/not detected as turbid.


For marine, aerosol and path reflectances at 412 nm mean differences and standard deviations have been computed for each MERIS data pixels independently for stable, unstable, and all aerosol models. In most cases the mean differences are about zero for any reflectance value and the standard deviations show strong dependencies on the values of the reflectances with increasing uncertainty for decreasing reflectances.

For marine reflectances at 412 nm we have shown that the uncertainty is larger in the case of unstable models and in the case of turbid waters.

By further sorting a statistics of 40 half-orbits per couples and geometry classes we have shown that the uncertainty depends on the couple with very distinct behaviour of diagonal and non-diagonal couples. Diagonal couples exhibit smaller standard deviations and appear more stable with regard to a change in geometry. The reason for this discrepancy lies in the propagation of aerosol properties from the NIR domain down to the visible domain: only one aerosol model is used in the case of diagonal couples while the final solution in the case of non-diagonal couples consists of a mixture of two aerosol models.

Computation of output uncertainties from noise simulation is very time consuming. A method for the estimation of these uncertainties is proposed, it uses Look-up-tables. These tables will be built once and for all and called during data retrieval for faster error estimation. A preferred method is based on the equation linking  $\text{Var}(\rho_w)$  and  $\text{Var}(\rho_{\text{pathstar}})$ ,  $\text{Var}(t)$ , and  $\text{Cov}(\rho_{\text{pathstar}}, t)$  as it directly relates the error in the NIR to output reflectances at other wavelengths.

We have tested the tabulation of the relationships between these quantities and the aerosol optical depth by a comparison between computed and simulated uncertainties. This comparison shows that  $\text{Var}(\rho_w)$  is accurately determined by the use of the LUTs in the case of stable aerosols over case 1 waters (see again Figure 29 and Figure 30).

	SENTINEL-3 OPTICAL PRODUCTS AND ALGORITHM DEFINITION  ERROR PROPAGATION IN THE ATMOSPHERE CORRECTION	REF: S3-L2-SD-01-C01-ACR-TN VERSION: 1.2 DATE: 30 SEPTEMBER 2010 PAGE 49
---	---	---

When considering all cases (stable + unstable) the uncertainty computed using the LUTs overestimates the actual error of about 25 %. As the retrieval cannot distinguish between stable and unstable cases the uncertainty computed using the LUTs can be used as a higher boundary for the error.

The consideration of turbid waters leads to an underestimation of the error of about 25 % when it is estimated with the LUTs. Our method is however not specifically designed for these cases and the consideration of turbidity flags in the retrieval allows caution on that matter.

In conclusion, marine reflectance errors induced by the propagation of input errors in the two NIR channels at 775 and 865 nm can accurately be estimated by the use of Look-Up Tables. These LUTs are determined once and for all for a specific input noise and will be called in the retrieval for a fast error computation.